Optical tweezers

Chapter · November 2017

1 author:

Marco Capitanio
European Laboratory for Non-Linear Spectroscopy
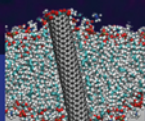**94** PUBLICATIONS **968** CITATIONS

Some of the authors of this publication are also working on these related projects:

Project   Mechanochemistry of myosin molecular motors View project
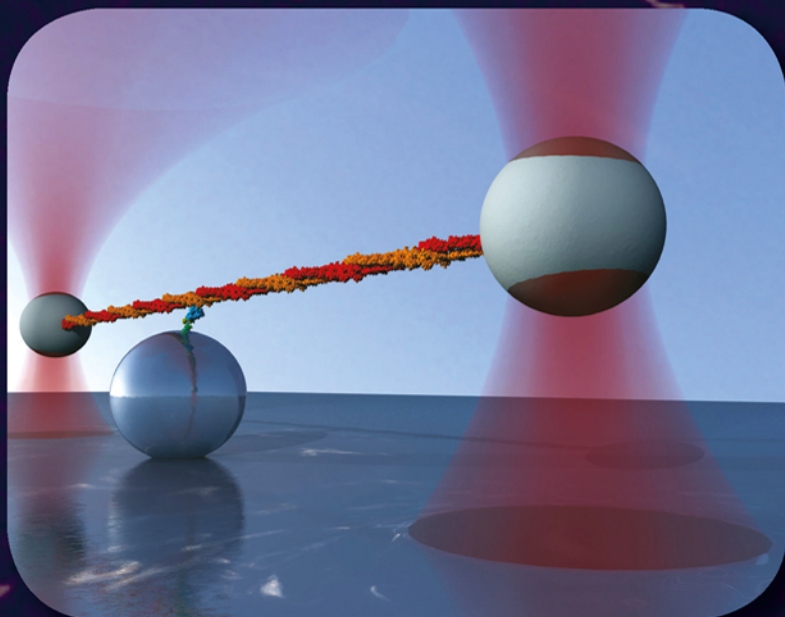
Project   Single molecule manipulation and imaging View project

EDITED BY YURI L. LYUBCHENKO

An Introduction to
SINGLE MOLECULE
BIOPHYSICS

5 Optical Tweezers

Marco Capitanio
University of Florence
Florence, Italy

Contents

5.1   Introduction

In 1986, when Arthur Ashkin and coworkers first reported about the single-beam gradient force optical trap, now referred to as optical tweezers, they could not imagine that they had invented what now has become one of the most widely used tools in single molecule biology (Ashkin et al. 1986). In the last two decades, optical tweezers have opened up the possibility to manipulate biological molecules and measure protein conformational changes and enzyme kinetics, one molecule at a time. The capacity to apply and measure forces from a few tens of femtonewtons to about 100 piconewtons, which well overlap with the range of forces experienced by biological molecules in their native environment, has elected optical tweezers as an ideal single molecule tool for the study of the mechanical properties of motor proteins and biological polymers, and for investigating regulation of biological systems by mechanical stress. In the last years, force has emerged as a fundamental regulatory factor for biological systems and the conversion of mechanical forces into biochemical signals has been discovered to be at the base of many biological processes fundamental for the development and differentiation of cells (Wozniak and Chen 2009), for their correct function, and for the development of pathologies (Jaalouk and Lammerding 2009). At the molecular scale, force modulates enzymatic activity, induces structural changes in proteins and nucleic acids, alters kinetics of molecular bonds (Marshall et al. 2003; Cecconi et al. 2005), regulates motions of molecular motors (Rief et al. 2000; Reconditi et al. 2004), and has a role in mechanical transduction and sensory functions (Laakso et al. 2008). All these processes are ultimately related to the capacity of force to modulate lifetimes of molecular interactions and transition rates in biochemical reaction cycles that involve motion (Howard 2001). Optical tweezers have been shown to be an ideal tool for the study of these dynamic processes owing to their high spatial and temporal resolutions. In particular, the last few years have seen major improvements in optical tweezers resolution, thus extending the range of measurable quantities and biological systems that can be interrogated with force (Capitanio and Pavone 2013).

Optical tweezers are easily implemented in an optical microscope by focusing a laser beam through the microscope objective to create a large gradient of light intensity. Dielectric microparticles are stably trapped near the beam focus owing to the interaction between the light intensity gradient and the particle itself. A polystyrene or silica microsphere is usually trapped and used as a handle to manipulate single biological molecules bound to it. The bead position is used to probe movements of molecular motors or conformational changes of proteins bound to the bead itself, while the force applied to the biological molecule is simultaneously measured.

In this chapter, we first illustrate how trapping forces are generated, describe how force and displacements are measured, and describe the mechanical behavior of microspheres trapped in optical tweezers. Since trapped microspheres are used as handles to manipulate biological molecules, their mechanical properties influence the outcome of biological measurements. Understanding their behavior when trapped in optical tweezers is thus essential to design and interpret experiments on biomolecules (Section 5.2). We then report in detail some of the prototypical optical tweezers configurations developed to date to investigate single biological molecules, with particular emphasis on recent applications (Section 5.3). We discuss factors affecting spatial and temporal resolutions in the different configurations of measurement and how it is possible to measure subnanometer conformational changes with a microsecond temporal resolution (Sections 5.4 and 5.5). Next, we illustrate principles of instrument design to get a deeper understanding of potentialities and limitations of the technique and its possible implementations (Section 5.6). We finally review a few important applications of optical tweezers to biological problems, exploring combinations of optical tweezers and fluorescence microscopy and outlining applications of optical tweezers in living cells (Section 5.7).

5.2   Principles of Optical Tweezers Trapping

5.2.1   Forces in Optical Tweezers

Forces in optical tweezers arise from the interaction of the laser light with the trapped dielectric particle. Scattering of the trapping light by the dielectric particle alters the photon flux and the momentum carried by the light. For the momentum conservation principle, an equal and opposite momentum change is imparted to the particle. Calculating optical forces in the general case is not a trivial task, but there are two limiting cases for which it becomes easier: the Rayleigh regime, when the particle dimension is much smaller than the wavelength of the trapping laser (Hulst 1981), and the ray optics regimes, for which the wavelength is much smaller than the particle size (Hecht 2002).

In the ray optics approximation, the laser beam can be decomposed into light rays that propagate in straight lines in media of uniform refractive index, carry momentum parallel to the ray direction, and are refracted at the boundary between two media with different refractive index following Snell's law. Figure 5.1a shows how a single light ray is refracted by a microsphere (commonly named *bead*) when the refractive index of the bead is bigger than that of the surrounding medium. The figure also shows how the light ray momentum $\mathbf{p_{in}}$ is changed and the force on the bead $\mathbf{F} = -\mathbf{dp}/\mathbf{dt}$, is generated, as dictated by the momentum conservation principle. The tightly focused beam that constitutes optical tweezers can be decomposed into ray pairs, each with appropriate intensity and direction, as illustrated in Figure 5.1b and c. For each pair, the light rays refracted by the trapped microsphere, the change in momentum, and net force can be drawn. Whatever the position of the bead with respect to the laser beam, the optical force is shown to point toward the beam focus. This qualitative description shows how stable three-dimensional trapping is achieved for this
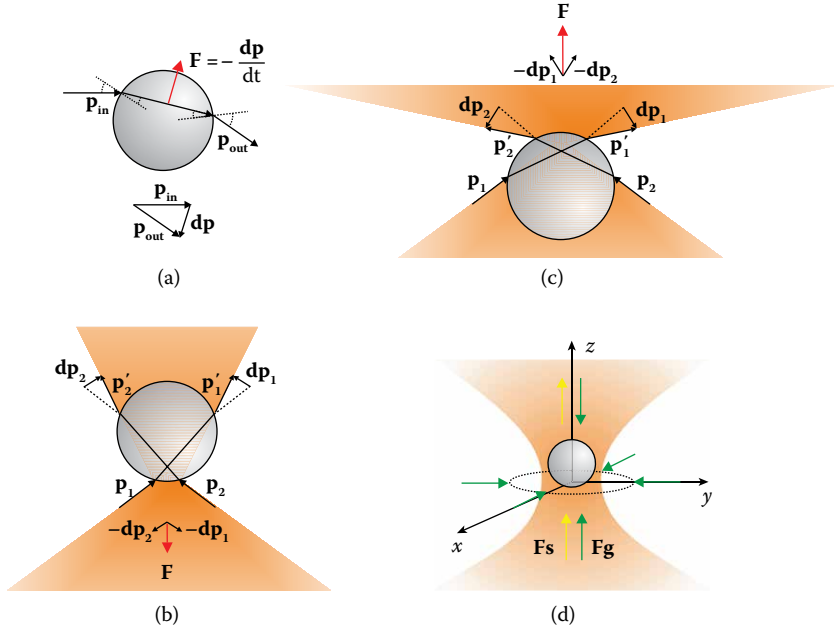
Figure 5.1 (a) A single light ray is refracted two times when it passes through a dielectric sphere. $\mathbf{p}_{in}$ and $\mathbf{p}_{out}$ are the incoming and outcoming momentum, respectively. $\mathbf{dp}$ is the vector difference $\mathbf{p}_{out} - \mathbf{p}_{in}$. $\mathbf{F}$ is the optical force applied to the dielectric sphere. The picture represents refraction when the refractive index of the sphere is bigger than that of the surrounding medium. (b and c) A focused trapping laser propagates upward and is refracted by a trapped microsphere positioned above (b) or below (c) the beam focus. The figure shows a pair of light rays symmetric with respect to the beam axis and, for each ray, the refracted ray and the change in momentum. The optical force due to the ray pair, represented in red, moves the bead toward the beam focus, whatever the position of the bead with respect to the laser beam. This picture can be generalized to cases in which the bead is positioned off-axis. (d) Force distribution in optical tweezers. The gradient force (green) points toward the beam focus, whereas the scattering force (yellow) points toward the direction of laser propagation.

geometry. Moreover, trapping forces can be appropriately quantified in the ray optics regime taking into account refraction, reflections, and changes in polarization at dielectric interfaces according to the usual Fresnel formulas (Ashkin 1992). This analysis shows that the force on a dielectric microsphere can be divided into two components: a *scattering force* component pointing in the direction of the incident light and a *gradient force* component pointing in the direction of the gradient of light intensity (Figure 5.1d). The distinction between scattering and gradient forces also emerges naturally in the Rayleigh regime, where the particle acts as a simple point dipole (Neuman and Block 2004), and it is a convenient

picture to analyze the trapping stability of optical tweezers. In fact, stable trapping is achieved when the gradient force, which pushes the bead toward the laser focus, predominates over the scattering force, which pushes the bead away in the direction of propagation of the beam. Therefore, the beam convergence angle should be as large as possible in optical tweezers to maximize the light intensity gradient, which is achieved by using large numerical aperture objectives and slightly overfilling the objective back aperture (Neuman and Block 2004).

Several articles, reviews, and books describe in detail the physics of the interaction between light and dielectric particles and accurately quantify forces applied by optical tweezers in the Rayleigh and ray optics regimes, as well as in the intermediate case in which the dimension of the bead is comparable to the light wavelength (Hulst 1981; Ashkin et al. 1986; Ashkin 1992; Wright et al. 1994; Ren et al. 1996; Neuman and Block 2004). A common feature of all regimes is that, for small distances, the trap behaves as a Hookean spring with an elastic constant k, the *trap stiffness*. For the purpose of this book, we therefore describe the force experienced by the bead (F_{trap}) as pointing toward the trap center and growing linearly with the distance of the bead center from the trap center (x): $F_{trap} = -k \cdot x$ (Figure 5.2a). The trap stiffness is constant in the axial plane (perpendicular to laser propagation) and smaller in the longitudinal direction owing to the smaller intensity gradient along that direction (Capitanio et al. 2002). Since in most optical tweezers geometries the force is applied in the axial plane (Section 5.3), in the present text we indicate a direction in this plane as x, unless otherwise specified. Beyond the linear region, a small zone of near-constant force follows at the border of the potential well, after which the force rapidly drops to zero (Figure 5.2b). Optical tweezers stiffness varies with laser power, beam focusing (i.e., the numerical aperture of the objective), bead dimension, and the refractive index of the bead and the surrounding medium. Several articles describe the dependence of tweezers force on those parameters. Table 5.1 shows typical stiffness values as a function of laser power and bead dimensions, which are the two parameters that can be more easily adjusted to match the experimental needs. In particular, since the gradient of the trapping
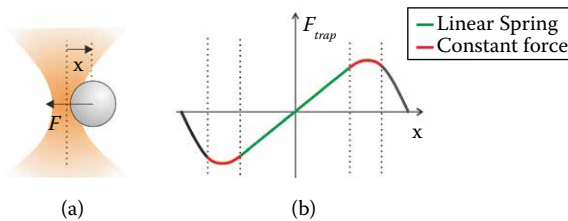
Figure 5.2 Force exerted by optical tweezers. (a) A dielectric microsphere is stably trapped near the laser beam focus. A lateral displacement of the bead (x) is opposed by a restoring force F_{trap}. (b) For small displacements of the bead from the trap center, the force grows linearly with x. Beyond the linear region, a near-constant force region follows, after which the force rapidly drops to zero.

Table 5.1 Trap Stiffness (k) and Position Detector Conversion Factor (β) as a Function of Laser Power and Bead Diameter

Laser Power (mW)	Bead Diameter (μm)	k (pN/nm)	β (nm/V)
3.2	1	0.024	50
8		0.05	
16		0.091	
32		0.18	
48		0.27	
3.2	0.5	0.01	270
	1	0.024	50
	2.6	0.004	125
	5	0.002	330

Source: Capitanio M, et al. *Review Sci Instrum* 73:1687–1696, 2002.

light intensity is proportional to the light intensity itself, tweezers stiffness grows proportionally to laser power. On the contrary, the dependence of stiffness on bead diameter is nonlinear and shows a maximum for bead dimensions close to the trapping light wavelength (Capitanio et al. 2002). Box 5.1 describes common methods to measure the bead position x, quantify the tweezers stiffness k, and, thus, measure forces and displacements in optical tweezers.

Box 5.1   Measuring Forces and Displacements in Optical Tweezers

Most of optical tweezers' success comes from their capacity to precisely measure the size of protein conformational changes and quantify forces applied by enzymes or biological polymers. Movements produced by biological molecules can be measured from the displacement of the attached bead through the use of position photodetectors (see Section 5.6.3). To this end, however, the photodetector voltage signal (V) must be first converted into a position signal (x). Analogously, to measure forces (F_{trap}), we need to know how the force applied on the bead is related to the measured bead displacement (x). In other words, we need two calibration curves $x(V)$ and $F_{trap}(x)$ to measure displacements and forces in optical tweezers. Since both calibration curves are linear for typical bead displacements (±500 nm using a 1 μm diameter bead), optical tweezers calibration reduces to the acquisition of two calibration parameters, the *position detector conversion factor* β (or the *detector sensitivity* $\alpha = 1/\beta$), and the optical tweezers *stiffness k* (Capitanio et al. 2002):

$$x = \beta \cdot V \qquad (5.1)$$

$$F_{\text{trap}} = -k \cdot x \tag{5.2}$$

As mentioned in Section 5.2.1, optical tweezers stiffness changes with laser power, beam focusing, bead dimension, and the refractive index of the bead and the surrounding medium. The detector sensitivity mainly depends on the detection strategy adopted, on the photodetector and its electronics (which is discussed in Section 5.6.3), as well as on the bead properties. Similar to the tweezers stiffness, the detector sensitivity is maximal for bead dimensions close to the trapping light wavelength. Table 5.1 shows typical detector sensitivity as a function of bead diameter. Several strategies have been developed for optical tweezers calibration, each one with peculiar advantages and drawbacks. Several articles and reviews describe the different calibration methods and how calibration parameters change with the bead and the trapping laser properties (Ghislain et al. 1994; Gittes and Schmidt 1998b; Capitanio et al. 2002). Free downloadable software for optical tweezers calibration is also available (Hansen et al. 2006; Osterman 2010).

Optical tweezers calibration is most commonly based on the analysis of thermal fluctuations of a trapped bead, which are discussed in detail in Section 5.2.2.2. For example, by applying the equipartition theorem as in Equation 5.9, we can obtain the trap stiffness by simply measuring the variance of the bead position:

$$k = \frac{k_B T}{\langle x^2 \rangle}, \tag{5.3}$$

where k_B is the Boltzmann constant, and T is the absolute temperature. However, to this end, we should be able to measure bead displacements, which is usually not the case unless the position detector conversion factor β has been, somehow, previously obtained. Frequency analysis of the thermal fluctuations of the trapped bead can be used to get both k and β. The power spectrum of the position signal V can be obtained from the power spectrum of bead thermal fluctuations $S_x(f)$, as described in Equation 5.11, and from Equation 5.1,

$$S_V(f) = \frac{1}{\beta^2} S_x(f) = \frac{1}{\beta^2} \frac{k_B T}{\pi^2 \gamma \left(f_C^2 + f^2 \right)} \tag{5.4}$$

where γ is the hydrodynamic drag coefficient, and $f_c = k/2\pi\gamma$ is the cutoff frequency (see Section 5.2.2.2). The β^2 term derives from the fact that the power spectrum is the squared Fourier transform of the bead position noise. The two calibration parameters k and β can thus be easily obtained by fitting Equation 5.4 to the experimental power spectrum of the position detector signal V recorded from a trapped bead, leaving k and β as free parameters (Figure 5.3).
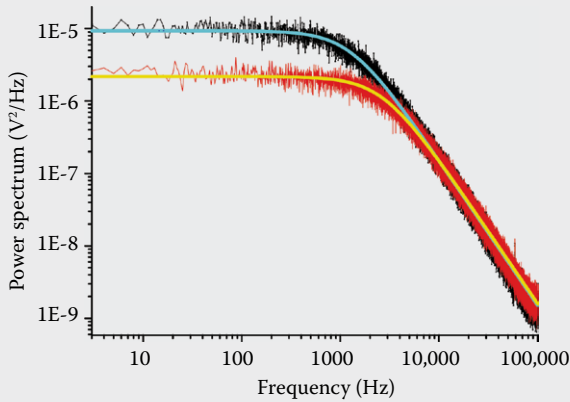
Figure 5.3 Power spectra of a 510 nm diameter bead trapped in optical tweezers. Each trace is the average of 30 power spectra obtained from 1 second recording acquired at 200 kHz. Data are fitted with Equation 5.4; from the fit, we obtain a cut-off frequency f_c of 1273 and 2703 Hz for the black and red curves, respectively, which correspond to trap stiffnesses of 0.04 pN/nm and 0.08 pN/nm, respectively. The nm/V conversion factor β is 75 nm/V from both calibrations. (From Capitanio M, et al. *Review Sci Instrum* 73:1687–1696, 2002.)

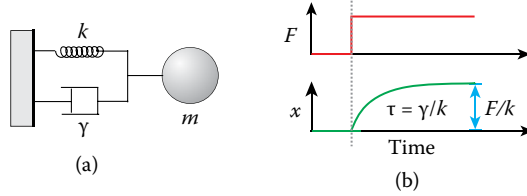### 5.2.2   Dynamics of a Trapped Bead in Optical Tweezers

Understanding how a bead moves when trapped in optical tweezers is fundamental to decipher experiments performed on single biological molecules, measure the amplitude and dynamics of protein conformational changes, optimize temporal and spatial resolution, and calibrate position detector sensitivity and trap stiffness (see Box 5.1). The simple mechanical model of a bead trapped in optical tweezers that we develop in this chapter is later extended to more complex configurations, including attached proteins and multiple optical tweezers. Here, we limit our analysis to the motion of the bead in one direction (*x*); extension to two or three dimensions can be easily derived.

The mechanical system considered here is represented in Figure 5.4a. The trapped microsphere is regarded as a point-like mass *m*, which is subjected to external forces from the optical tweezers, represented as a spring, and from a viscous buffer in which it is immersed, represented as a dashpot.

As introduced in the preceding paragraph, optical tweezers can be regarded as a Hookean spring, which exerts a force directly proportional to the spring extension *x*:

$$F_{trap} = -kx \tag{5.5}$$

where *k* is the *trap stiffness*.

Figure 5.4 (a) Mechanical model of a microsphere of mass m, trapped in optical tweezers with stiffness k, and immersed in a viscous solution with drag coefficient γ. (b) Dynamics of the microsphere after a force step F. The bead exponentially moves from $x = 0$ to the new equilibrium position $x = F/k$ with a time constant $\tau = \gamma/k$. Inertial terms are neglected in the approximation of low Reynolds numbers.

An object that is moving inside a viscous fluid with velocity v experiences a force opposing its motion. For small objects, such as the micrometer-sized bead considered here, cells, or proteins in water solution, the viscous force is always predominant over the inertial force (i.e., the object mass m times its acceleration). The ratio between inertial and viscous force is called the Reynolds number (Re), and Re < 1 for small objects. Small Reynolds numbers imply that the fluid flow is laminar and the viscous force is proportional to velocity (Batchelor 1967; Howard 2001), as stated by Stokes' law:

$$F_{drag} = -\gamma v \tag{5.6}$$

where γ is the *hydrodynamic drag coefficient*. The drag coefficient depends on the shape of the object and on the fluid viscosity (η). For a sphere of radius R far from any surface, we get $\gamma = 6\pi\eta R$ (Batchelor 1967).

The equation of motion of the bead in one direction (x) can be obtained after applying Newton's second law:

$$\gamma \frac{\partial x}{\partial t} + kx = F \tag{5.7}$$

where F is the additional external force acting on the bead in x-direction, and we have neglected the inertial term $m = \dfrac{\partial^2 x}{\partial t^2}$ in the approximation of low Reynolds numbers.

5.2.2.1   Motion After a Perturbation

We first describe the motion of the trapped bead after a perturbation by an external force. This can happen, for example, when a protein attached to the bead undergoes a conformational change. Next, we see that the bead motion depends on both trap stiffness and viscous damping on the bead.

Let's assume that the bead is at rest at time 0 in the center of the trap (i.e., $x(0) = 0$, where the spring is relaxed), and a constant external force F puts the system out of equilibrium. At time 0, the bead starts moving at constant velocity $\frac{\partial x}{\partial t} = \frac{F}{\gamma}$, as described by Equation 5.7. The spring then elongates in the direction of the force, applying an increasing opposing force, and the bead velocity consequently decreases, until it drops to zero. The system, thus, reaches a new equilibrium position in which the elastic force equals the external force: $kx = F$. The time course of this motion can be obtained by solving the differential Equation 5.7. We get:

$$x(t) = \frac{F}{k}\left[1 - \exp\left(-\frac{t}{\tau}\right)\right]; \tau = \frac{\gamma}{k} \tag{5.8}$$

This motion is represented in Figure 5.4b. The time constant τ is named the *relaxation time* and is a fundamental characteristic of the system, which tells us the time required by the trapped bead to reach the new equilibrium position. The relaxation time sets a limit in the time resolution of optical tweezers. It is not possible to detect protein dynamics faster than the relaxation time, simply because the bead dynamics occur with a time constant that is dictated by the relaxation time. Table 5.2 shows typical relaxation times of trapped beads in typical optical tweezers configurations, some of which are described in Section 5.3. In the case considered here (single-bead configuration in Table 5.2), we get $\tau \sim 0.1$ ms for a 1 µm diameter bead trapped in optical tweezers with typical stiffness (0.1 pN/nm). We should, however, point out that the relaxation time changes significantly when the bead is tethered to the coverslip surface through an attached protein, which can increase significantly the system stiffness. A 1 µm bead bound to a protein with typical stiffness ($k = 1$ pN/nm), shows a relaxation time of about 10 µs (see Table 5.2, Single bead + kinesin). We discuss this point in detail in Section 5.5, when we analyze the temporal resolution of optical tweezers in typical experimental configurations.

Table 5.2 Relaxation Time versus Stiffness and Bead Diameter for Different Configurations of Measurement in Optical Tweezers

System	Bead Diameter (µm)	System Stiffness (pN/nm)	Relaxation Time (µs)
Single bead	1	0.1	94
	0.2		19
Rigid dumbbell	2×1	2×0.025	377
	2×0.5		188
Single bead + kinesin	1	1	9.4
	0.2		1.9
Rigid dumbbell + myosin	2×1	1	19
	2×0.5		9.4

5.2.2.2 Thermal Fluctuations of a Trapped Bead

In the previous paragraph, we examined the dynamics of a trapped bead subjected to an external force F. However, we did not take into account thermal forces, which strongly affect the motion of micrometer-sized beads immersed in water solution at room temperature. We now analyze the motion of the trapped bead subjected to thermal forces only.

Under this assumption, F in Equation 5.7 represents the fluctuating force originated by random collisions of water molecules with the trapped microsphere. Because of the stochastic nature of the resulting motion, the bead position can be analyzed in statistical terms only—that is, by measuring the probability $p(x)$ of finding the bead in position x or by calculating average position values such as the mean position $\langle x \rangle$ or the mean square position $\langle x^2 \rangle$.

The trapped bead randomly oscillates about position $x = 0$, which is the bead equilibrium position where the spring is relaxed (see Figure 5.5a, left). Therefore, $\langle x \rangle = 0$, as can be easily inferred from the symmetry of Equation 5.7 with respect to the equilibrium position. In this case, the mean square position $\langle x^2 \rangle$ equals the position noise variance $\sigma_x^2 = \langle (x - \langle x \rangle)^2 \rangle$. This quantity is an important parameter that quantifies how much the trapped bead oscillates because of thermal forces. The equipartition theorem gives us a simple way to calculate $\langle x^2 \rangle$ (Landau et al. 1980). For an object in a harmonic potential $U(x) = \frac{1}{2}kx^2$:

$$\frac{1}{2}k_B T = \frac{1}{2}k\langle x^2 \rangle \implies \langle x^2 \rangle = \sigma_x^2 = \frac{k_B T}{k} \tag{5.9}$$

where k_B is the Boltzmann constant and T the absolute temperature. Equation 5.9 is telling us that bead thermal fluctuations increase with temperature and decrease when restrained by a trap with higher stiffness, a quite intuitive result represented in Figure 5.5a.

At thermal equilibrium, we can also derive $p(x)$ from Boltzmann distribution (Landau et al. 1980; Howard 2001):

$$p(x) = \frac{1}{Z}\exp\left[-\frac{U(x)}{k_B T}\right] = \frac{1}{Z}\exp\left(-\frac{x^2}{2\frac{k_B T}{k}}\right) \tag{5.10}$$

where $Z = \int_{-\infty}^{+\infty} \exp\left[-U(x)/k_B T\right]dx$ is a normalizing constant, called the partition function, which assures that the sum of all probabilities adds up to one (Landau et al. 1980). Equation 5.10 tells us that thermal noise is Gaussian distributed, with $\langle x \rangle = 0$ (Figure 5.5a, right). From Equation 5.10, we also find that the variance of the Gaussian distribution is $\sigma_x^2 = \frac{k_B T}{k}$, which confirms Equation 5.9 obtained from the equipartition theorem.
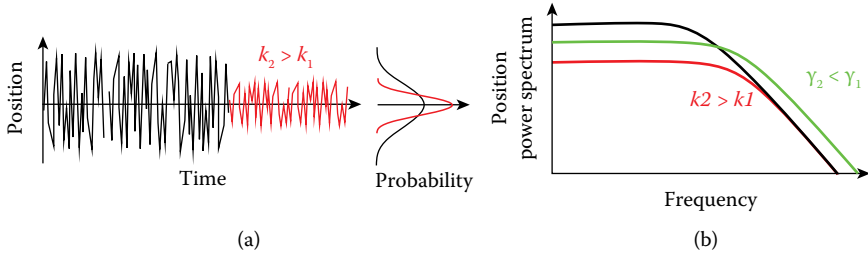
Figure 5.5 (a) Position fluctuations of a trapped bead owing to thermal noise. *Left*: Amplitude of position fluctuations depends on the trap stiffness according to Equation 5.9. *Right*: Position noise is Gaussian distributed, as described by Equation 5.10. (b) Frequency distribution of position noise represented in a log–log scale. From Equation 5.11, position fluctuations decrease with stiffness k at low frequency ($f \ll f_C \Rightarrow S_x(f) = 4k_BT\gamma/k^2$), but not at high frequency ($f \gg f_C \Rightarrow S_x(f) = k_BT/\pi^2\gamma f^2$), as represented by the black and red traces. Position fluctuations decrease with the drag coefficient γ for low frequency, but conversely, they increase for lower values of γ at high frequency, as represented by the black and green lines.

Equations 5.9 and 5.10 fully describe thermal noise amplitude at equilibrium. However, it is also important to know that thermal noise amplitude varies depending on the time (or frequency) scale considered, and largely decreases at high frequencies. This has important implications when studying dynamic processes occurring at different time scales, as shown later. The power spectrum of the bead position (i.e., the squared magnitude of its Fourier transform) describes how noise amplitude changes with frequency (Gittes and Schmidt 1998a; Neuman and Nagy 2008):

$$S_x(f) = \frac{k_BT}{\pi^2\gamma\left(f_C^2 + f^2\right)} \tag{5.11}$$

where $f_C = k/2\pi\gamma = 1/2\pi\tau$ is the *cut-off frequency* of the motion, and it is inversely proportional to the relaxation time of the trap defined in Equation 5.8. The position variance σ_x^2 in a given frequency range can be simply obtained as the area (integral) under the power spectrum in that frequency range (Landau et al. 1980; Neuman and Nagy 2008). Equation 5.11 implies that noise amplitude is constant for frequencies well below the cut-off frequency ($f \ll f_C$) and decreases as $1/f^2$ for high frequencies ($f \gg f_C$), as depicted in Figure 5.5b (in the log–log scale of the graph, $1/f^2$ becomes a line with slope –2). The position variance σ_x^2 over all frequencies can be obtained as the total area (integral) under the power spectrum described by Equation 5.11, which gives us again Equation 5.9: $\sigma_x^2 = k_BT/k$.

The presence of the cut-off frequency in thermal noise is a consequence of the relaxation time of bead motion. In fact, since bead movements cannot occur at time scales shorter than the relaxation time, collisions with water molecules

occurring at these short time scales are not transformed into significant bead movements, and thermal noise is consequently reduced.

We also observe that both trap stiffness k and bead dimension R ($\gamma = 6\pi\eta R$) affect the position noise amplitude through the cut-off frequency of motion. A higher stiffness determines a decrease of the noise amplitude at low frequencies. On the contrary, smaller beads cause a reduction of the noise amplitude at low frequencies, but an increase at high frequencies, so that the total noise in Equation 5.9 is not dependent on bead dimension (Figure 5.5b).

In the more general case in which the bead is subjected to both thermal forces and a constant external force, the overall motion is a directed motion described in the previous paragraph by Equation 5.8 superimposed to the random motion described in the present paragraph.

5.3   Configurations of Measurement

5.3.1   Single-Bead Geometry

In the simplest optical tweezers geometry, named *single-bead* or *single-trap geometry*, optical tweezers are kept at a fixed position and a trapped bead monitors conformational changes and movements of a protein, which is linked on one end to the bead and on the other end to the coverslip surface (Figure 5.6a). This configuration has been largely used to investigate processive molecular motors such as conventional kinesin (Svoboda et al. 1993), which can move continuously

(a)   (b)   (c)
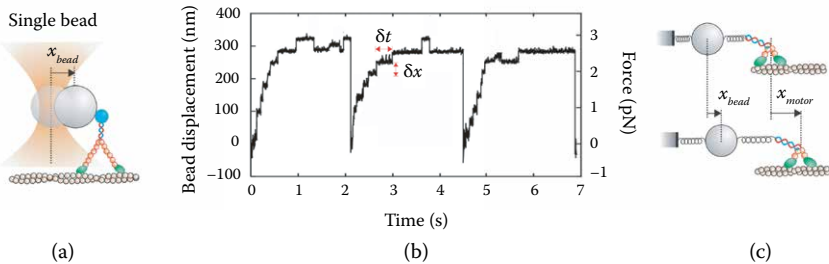
Figure 5.6 Single-bead or single-trap geometry. (a) The drawing represents a myosin V molecule attached to a trapped bead and proceeding along an actin filament stuck on the coverslip surface. The optical trap position is fixed and the bead displacement x_{bead} measures protein displacement. (b) An example showing stepwise movement of a single myosin Va motor in a single-bead assay. Consecutive 36 nm stepwise movements (δx) and dwell times between steps (δt) are clearly visible. Backward steps are also visible at high force. The force was calculated from the displacement of the bead from the trap center times trap stiffness (0.009 pN/nm; right axis). Stall force is about 2.5 pN. (Adapted from Uemura, S., et al., *Nat. Struct. Mol. Biol.*, 11, 877–883, 2004. With permission.) (c) Measured bead displacements (x_{bead}) do not correspond to motor displacements (x_{motor}) but depend on the motor protein displacement and on the values of the trap and protein stiffness.

along a microtubule for up to several microns, or myosin Va (Uemura et al. 2004), which proceeds along actin filaments. In this configuration, the force applied to the processive motor increases as the protein displaces the bead from the trap center while translocating along its track ($F_{trap} = -k_{trap}x_{bead}$; in the following, we specify stiffness k and displacements x with appropriate subscripts to avoid ambiguity). When the maximum force that the motor protein can develop is reached, the motor stalls (Figure 5.6b). Stall forces of kinesin (Svoboda and Block 1994), RNA polymerase (Yin et al. 1995), and many other motors have been measured using the single-bead geometry.

Moreover, various analysis approaches have been developed to detect the single steps from a position recording of a stepping motor (Carter et al. 2008). From such analyses, it is possible to measure the amplitude of the motor working stroke (the step δx in Figure 5.6b), as well as the distribution of dwell times between steps (δt), which gives us precious information on the kinetics of the mechanochemical cycle of the motor protein (Howard 2001).

Care must be taken when measuring molecular movements in an optical trap, since bead movements (x_{bead}) do not always correspond to the movements of the biological molecule (x_{motor}). In fact, the system is compliant owing to the finite stiffness of the trap (k_{trap}) and the molecule and linkages connecting the molecule to the bead and to the coverslip surface (k_{motor}) (Figure 5.6c). When the motor takes a step, both springs are stretched, so that $x_{bead} \neq x_{motor}$. Referring to Figure 5.6c,

$$x_{bead} = x_{motor} \frac{k_{motor}}{k_{motor} + k_{trap}} \tag{5.12}$$

so that $x_{bead} = x_{motor}$ only when $k_{trap} \ll k_{motor}$. In general, it is important to evaluate both trap and motor stiffness and use Equation 5.12 to accurately determine the motor working stroke.

5.3.2 Two-Bead Geometry

Double optical tweezers (two-bead, double-trap, or dumbbell assay) or a single trap together with a micropipette have been widely employed to investigate the mechanical properties (force–extension curves) of single dsDNA and ssDNA molecules (Smith et al. 1996), as well as single RNA molecules (Liphardt et al. 2001). In this configuration, one of the two traps is held at a fixed position and probes force applied to the polymer, while the second trap or the micropipette is displaced to stretch the polymer and measure its force–extension curve (Figure 5.7a, top). The force–extension curve, which is a straight line for Hookean linear springs, can display complex behavior in biopolymers such as DNA (Figure 5.7a, bottom). Different regimes in the force–extension curve allow the deciphering of different conformational states of the polymer and changes in molecular structure (van Mameren et al. 2009).

More recently, the two-bead geometry has been applied to investigate protein folding by using dsDNA handles to tether the protein between the two beads (Figure 5.7b, top) (Cecconi et al. 2005; Gebhardt et al. 2010; Stigler et al. 2011). The force–extension curve of a single protein transitioning between folded and unfolded states can reveal intermediates conformations, interactions between
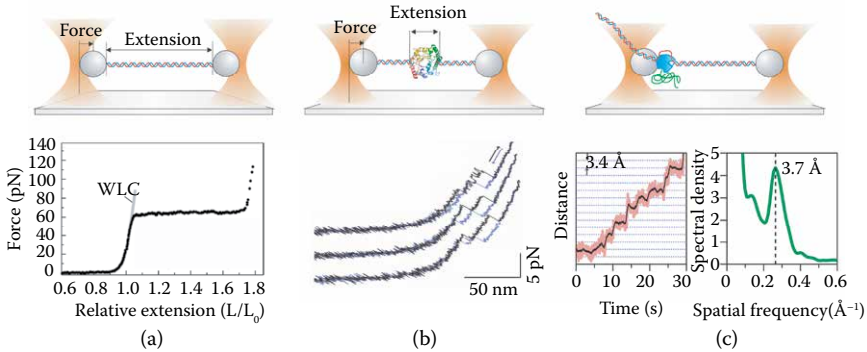
Figure 5.7 Two-bead or double-trap assay. (a) Measurement of force–extension curve of a biopolymer. *Top*: The left trap is stationary and measures the force applied to the polymer. The right bead moves in steps or ramps and, for each displacement, the force applied to the polymer and its extension are measured. *Bottom*: Typical force–extension curve of a 3′-3′ attached DNA, with free 5′ ends. The elastic properties of DNA below the overstretching force of 65 pN are well described by the extensible worm-like chain (WLC) model (*gray line*). At 65 pN, the DNA molecule undergoes the overstretching transition, during which the intrinsic contour length of the DNA increases from 100% to about 170%. (Adapted from van Mameren, J., et al., *Proc. Natl. Acad. Sci. U S A*, 106, 18231–18236, 2009. With permission.) (b) Probing unfolding–refolding of single proteins by force. *Top*: Analogous to panel (a), the left trap measures force while the right trap is moved to change protein extension. *Bottom*: Folding and unfolding of single calmodulin stretch-and-relax cycles for velocity $v = 500$ nm/s. (Adapted from Stigler, J., et al., *Science*, 334, 512–516, 2011. With permission.) (c) Dynamics of DNA-processing enzymes. *Top*: Cartoon represents a single, transcriptionally active molecule of RNA polymerase (RNAP, blue) attached to a bead held in a trap and tethered via the upstream DNA to another trapped bead. During elongation, the DNA tether lengthens and the beads move apart. *Bottom Left*: A representative record for a single RNAP molecule transcribing under 18 pN of assisting load, median-filtered at 50 ms (pink) and 750 ms (black). Horizontal lines (dotted) are spaced at 3.4 Å intervals. *Bottom Right*: The power spectrum of the average autocorrelation function derived from position histograms shows a peak at the dominant spatial frequency, corresponding to the inverse of the fundamental step size, 3.7 ± 0.6 Å. (Adapted from Abbondanzieri, E.A., et al., *Nature*, 438, 460–465, 2005. With permission.)

protein domains, and energy landscape, which provides a conceptual framework for understanding protein folding (Figure 5.7b, bottom).

The same geometry has been largely used to monitor DNA and RNA processing enzymes, such as the bacteriophage φ29 (Smith et al. 2001b; Chemla et al. 2005), T7 DNA polymerase (Wuite et al. 2000), RNA polymerases (Abbondanzieri et al. 2005; Fazal et al. 2015), helicases (Dumont et al. 2006; Garcia-Garcia et al. 2015), and the ribosome (Wen et al. 2008; Kaiser et al. 2011) (Figure 5.7c). In those

experiments, the molecular motor is usually attached to one of the trapped beads and is linked to the second bead through a DNA or RNA tether. The processive movements of the motor along the nucleic acid tether shorten or lengthen it, so that the motor movements can be detected through bead movements (Figure 5.7c, top). When properly optimized, this assay allows resolving single base-pair stepping of RNA polymerase (Abbondanzieri et al. 2005), as illustrated in detail in Section 5.4, where we discuss spatial resolution in optical tweezers (Figure 5.7c, bottom). Moreover, in this assay, enzyme processivity can be efficiently analyzed under constant force by using force-clamp techniques that we describe in Section 5.3.4.

5.3.3   Three-Bead Assay

In the three-bead assay, a biopolymer is suspended between two optically trapped beads, and a binding protein is attached to a third bead stuck onto the coverslip (Figure 5.8a). This configuration has been extensively used to investigate nonprocessive molecular motors such as skeletal, cardiac, and smooth muscle myosin (Finer et al. 1994; Molloy et al. 1995; Capitanio et al. 2006). Nonprocessive molecular motors interact with their cytoskeletal filament for a single enzymatic cycle during which they produce a conformational change (working stroke) and unbind.

Position recordings from a single skeletal muscle myosin interacting with actin appear as in Figure 5.8b (Capitanio et al. 2006). When myosin is not bound to actin, the dumbbell oscillates within the traps because of thermal motion, the amplitude of the oscillations depending on the overall system stiffness, as described by Equation 5.9. When myosin binds to actin, the system stiffness increases, and position noise consequently decreases. Acto-myosin interactions

(a)   (b)
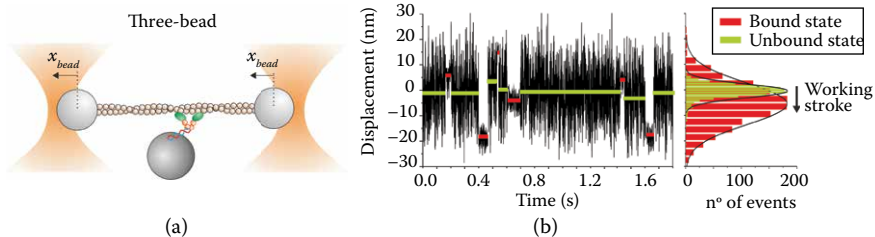
Figure 5.8 Three-bead assay. (a) Cartoon illustrates an actin filament connected to polystyrene beads held by optical tweezers. A single myosin molecule is attached onto a third bead stuck to the coverslip surface. Movements of the actin filament produced by the attached myosin are measured through bead displacements (x_{bead}) (b) *Left*: Position recording while myosin is interacting with actin. Red and green lines indicate the average position of bound and unbound events, respectively. *Right*: Distributions of the average position of bound and unbound events of a 100 s position recording containing several hundreds of interactions. The working stroke is obtained from the displacement between the centers of the two distributions. (Adapted from Capitanio, M., et al., *Micr. Res. Tech.*, 65, 194–204, 2004. With permission.)

are thus detected from noise reduction of the bead position signal (red lines in Figure 5.8b). Various methods have been developed for the separation of low-variance events (bound state) from high-variance events (unbound state) (Knight et al. 2001; Smith et al. 2001a). Since myosin displaces the actin filament very rapidly after binding (~1 ms) and interactions last for several tens of milliseconds at the low ATP concentrations used in these experiments, the position of bound events corresponds here to the position after the working stoke is completed. Therefore, myosin working stroke can be evaluated from the displacement between the average position of bound and unbound events (Figure 5.8b, right). Moreover, the distribution of event duration describes the kinetics of the mechanochemical cycle of the myosin motor.

By replacing the actin filament with a microtubule, the three-bead assay has been adapted to study microtubule-based molecular motors such as cytoplasmic dynein (Walter et al. 2010, 2012) or ncd kinesin (deCastro et al. 2000). Alternatively, the same assay has been used to study DNA binding proteins (Capitanio et al. 2012) and processing enzymes (Skinner et al. 2004). The same assay was recently applied to investigate actin-binding proteins involved in mechanotransduction processes (Ren et al. 2009; Buckley et al. 2014). Some of the experiments reported here required dynamic trap configurations that are described in the next paragraphs.

5.3.4   Force Clamp

A more sophisticated geometry is the force clamp or isotonic clamp, which has been developed in the single-bead, two-bead, or three-bead geometries, using different strategies. In active force clamps, the distance between the bead and the trap (x_{bead}) is continuously monitored through a position detector (Visscher et al. 1999; Rief et al. 2000). As the distance changes owing, for example, to the movements of a motor protein, a feedback system rapidly moves the trap to keep the distance, and thus the force, constant ($x_{bead} = const. \Rightarrow F_{trap} = -k_{trap}x_{bead} = const.$) (Figure 5.9a, top). Active force clamps were extensively applied in a single-bead geometry to study processive molecular motors such as kinesin (Visscher et al. 1999), myosin Va (Rief et al. 2000), myosin VI (Rock et al. 2001), and RNA polymerase (Wang et al. 1998). In these experiments, the bead and the trap move together and probe protein movements (Figure 5.9a, bottom trace). Usual position detection methods, such as the back focal plane detection described in Section 5.6.3, directly measure the distance of the bead from the trap center (x_{bead}). Once the trap stiffness is known, the position detector is used to measure the force ($F_{trap} = -k_{trap}x_{bead}$), which is kept constant by the feedback loop (besides high-frequency thermal noise that cannot be compensated by the feedback because of its limited frequency response) and the feedback signal, i.e., the trap position (x_{trap}), measures protein movements.

A double-trap configuration, in which one trap is stationary and the other one is force-clamped, has been applied to study nucleic acids or protein folding (Liphardt et al. 2001; Gebhardt et al. 2010; Bianco et al. 2011; Rognoni et al. 2012) and movements of DNA and RNA processing enzymes (Kaiser et al. 2011; Fazal et al. 2015). Sometimes the stationary trap is replaced by a micropipette that holds one of the beads in a fixed position. Figure 5.9b shows how such a configuration
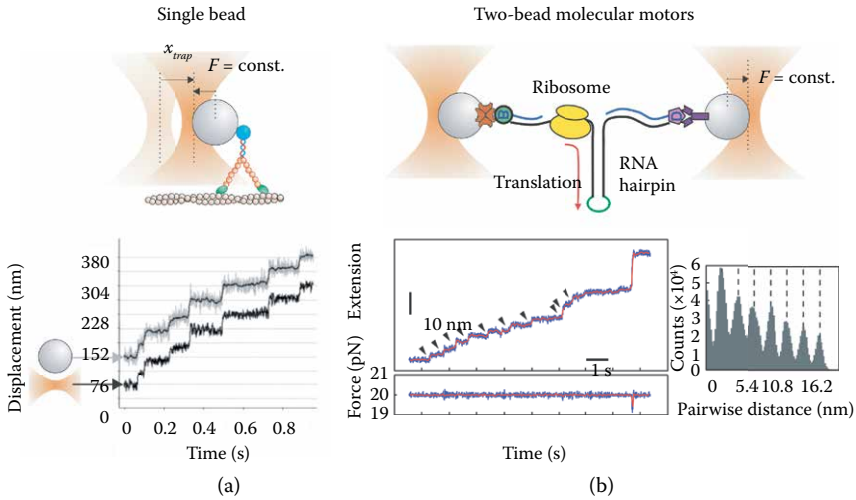
Figure 5.9 Force-clamp geometries. (a) Single bead. *Top*: The drawing represents a myosin-V molecule attached to a trapped bead, which proceeds along an actin filament stuck on the coverslip surface. A feedback system moves the trap to keep force on the bead and on the motor protein constant. Trap displacements (x_{trap}) measure protein displacements. *Bottom*: Example record of the bead position (gray curve) and trap position (lower black curve) as the myosin-V molecule steps along the actin filament. The distance between the two is kept constant by the feedback loop; thus, the myosin-V molecule is always kept under constant load. The thin black line within the gray curve is a filtered bead position signal (box filter, 15 ms). (Adapted from Rief, M., et al., *Proc. Natl. Acad. Sci. USA,* 97, 9482–9486, 2000. With permission.) (b) Two-bead force clamp applied to molecular motors. *Top*: Cartoon illustrating the experimental configuration used to study translation by a single ribosome. (Adapted from Wen, J.D., et al., *Nature,* 452, 598–603, 2008. With permission.) A single ribosome was stalled at the 59 side of the mRNA hairpin construct, which was then held between two polystyrene beads. The right bead applied a constant force below the force required to unfold the hairpin, and the extension change was monitored in time from the movements of the force-clamped trap. The static trap was substituted by a micropipette depending on the RNA construct used for translation. *Bottom left*: Extension and force trajectories during translation. The data were collected at 200 Hz (blue traces) and smoothed to 10 Hz (red). Discrete steps are indicated by arrowheads. The 18 nm rip at the end of the record corresponds to spontaneous opening of the remaining approximately 18 bp hairpin ahead of the translating ribosome. *Bottom right*: Pairwise distance analysis of the extension trajectory in the first 10 s of the record, after correction for drift, shows codon-by-codon stepping. *(Continued)*

Two-bead-RNA/protein folding

Three-bead-ultra-fast force clamp

(c)

(d)
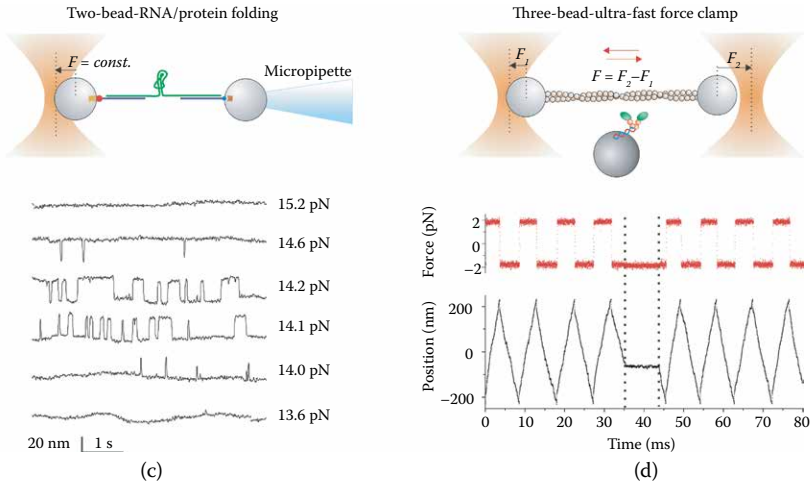
Figure 5.9 (continued) Force-clamp geometries. (c) Two-bead force clamp applied to RNA and protein folding. *Top*: The experimental configuration used to study reversible unfolding of a single RNA molecule under force (Liphardt et al. 2001). Individual RNA molecules (green) were attached to polystyrene beads by RNA/DNA hybrid "handles" (purple). One bead was held in a force-clamped optical trap, and the other bead was held by a micropipette. *Bottom*: Length versus time traces of the RNA hairpin at various constant forces. The end-to-end distance of the RNA hairpin hopped back and forth by 18 nm, signaling the repeated folding and unfolding of a single RNA molecule. By increasing the pre-set force, it was possible to tilt the folded-to-unfolded equilibrium toward the unfolded state (Liphardt et al. 2001). (d) Three-bead ultrafast force clamp. *Top*: Schematic of the operational principle illustrating constant force $F = F_2 - F_1$ applied to the dumbbell through two feedback systems clamping the force on the left bead to $-F_1$ and on the right bead to F_2. *Bottom*: Force and position of the dumbbell. The net force is switched between $+F$ and $-F$ ($F = 2pN$) to keep the dumbbell within a confined spatial interval (±200 nm). When myosin binds to actin, the force is transferred to myosin and the dumbbell stops (vertical dotted lines).

has been used to follow translation by a single ribosome, one codon at a time (Wen et al. 2008). Figure 5.9c depicts the experiment by Liphardt et al. in which they used mechanical force to induce the unfolding and refolding of a single RNA hairpin (Liphardt et al. 2001). The RNA hairpin could be mechanically unfolded and when kept at constant force within a critical force range, hopped between folded and unfolded states (Figure 5.9c, bottom trace).

A three-bead force clamp (named ultrafast force-clamp spectroscopy) was recently developed to study intermittently binding proteins such as nonprocessive molecular motors and transcription factors binding DNA under constant force (Capitanio et al. 2012) (Figure 5.9d). Here, a constant force is applied to the dumbbell through a double feedback system. The force is alternated back and forth so that the dumbbell oscillates in a triangular wave fashion when it is free

in solution. When the molecule binds the filament, the force is rapidly transferred to the molecule, and the dumbbell stops its movement (Figure 5.9d, bottom trace). Molecular interactions occur under the constant force imposed by the force clamp on the dumbbell. This technique has several advantages in terms of temporal resolution and is discussed in detail in Section 5.5.3, in relation with methods that allow pushing temporal resolution of optical tweezers to the limit.

Despite the higher complexity of implementing force clamps, single molecule data collected in this configuration allow a direct measurement of force dependence of conformational transition rates, thus enabling the reconstruction of the energy landscapes of molecular structural states. Force-clamp geometries also open up the possibility of measuring the mechanical output of molecular motors, such as the working stroke and the average distance traveled before dissociating (run length), as a function of load. This configuration also eliminates the complication of correcting the measured distances taking into account the compliances of the motor protein and its linkages with the bead and the coverslip surface (Equation 5.12). In fact, all elastic elements remain at a fixed stretching length under force clamp ($x_{bead} = F_{trap}/k_{trap} = const.$), and motor movements are precisely measured from the feedback signal ($x_{motor} = x_{trap}$).

As we see in Section 5.6, piezo or motorized mirrors can be used to steer the laser beam and move the trap, although much faster response (µs) can be reached using acousto-optic deflectors (AODs) (Lang et al. 2002) or electro-optic deflectors (EODs) (Valentine et al. 2008). The limited bandwidth of the feedback loop can sometimes be restrictive (Elms et al. 2012), depending on the time constant of the process under study relative to the response time of the feedback loop. Alternative configurations have been developed to overcome such limitation. For example, Nambiar et al. created a one-dimensional region of constant force extending over several micrometers by rapidly line scanning the trapping light while simultaneously modulating its intensity (Nambiar et al. 2004). Greenleaf et al. developed a passive all-optical force clamp exploiting the constant-force region of optical tweezers near the border of the potential well (Figure 5.2b) (Greenleaf et al. 2005). Such a clamp was successfully employed to measure the force-velocity relationship for transcription by RNA polymerase (Abbondanzieri et al. 2005) (Figure 5.7c), as well as folding trajectories of nucleic acids under constant force (Woodside et al. 2006; Greenleaf et al. 2008).

5.3.5 Position Clamp

Opposite to force clamp, where force on the protein is kept constant and protein movements are measured, the position clamp (also called the isometric clamp) prevents protein movements and measures the force that is developed. Molecular isometric clamp was first developed by Finer et al. to measure forces exerted by single actomyosin complexes in the three-bead geometry (Finer et al. 1994) and subsequently refined by Takagi et al. (2006). In this latter implementation, one of the two beads, termed the *transducer bead*, detects movements of the dumbbell, whereas the force on the other bead, the motor bead, is changed using an AOD to oppose the detected movements and maintain the bead-actin-bead assembly at its initial position (Figure 5.10a). Actin–myosin interactions are thus detected
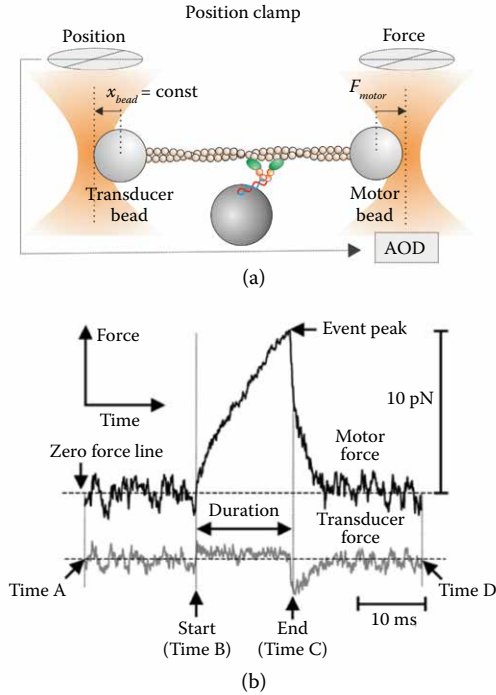
Figure 5.10 Position or isometric clamp. (a) The left bead detects movements of the dumbbell (x_{bead}), whereas the right bead moves using an AOD to oppose the detected movements. The right bead measures the force applied by the motor protein (F_{motor}). (b) A single acto-myosin interaction in the position clamp. After the force peak the force rapidly declines. The time between the start (Time B) and the point at which the rate of force declines is fastest (Time C) is defined as the duration of an episode. (From Takagi, Y., et al., *Biophys. J.*, 90, 1295–1307, 2006. With permission.)

from the increase in force exerted on the motor bead (Figure 5.10b). Myosin isometric force measured from these experiments was ~9 pN, close to that estimated from high-resolution fiber mechanics studies (Piazzesi et al. 2002). The same assay recently allowed the measurement of force-dependent interaction between actin and cardiac myosin (Greenberg et al. 2014) and different isoforms of myosin I (Laakso et al. 2008, 2010; Greenberg et al. 2012).

5.3.6 Dynamic Force Spectroscopy

Another strategy to probe the effect of force on molecular bonds is dynamic force spectroscopy (DFS), in which the distribution of rupture forces of molecular bonds is measured at different loading rates (Evans 2001) (Figure 5.11). Constant loading rates can be applied by moving the trapped bead at constant velocity ($dF_{trap}/dt = -k_{trap} \cdot [dx_{bead}/dt] = -k_{trap} \cdot v_{bead}$) (Arya et al. 2005; Dame et al. 2006; Guo and Guilford 2006; Bianco et al. 2007; Lewalle et al. 2008; Pyrpassopoulos et al. 2010), or by clamping the position of the bead relative to the optical trap ($x_{bead} = const.$)
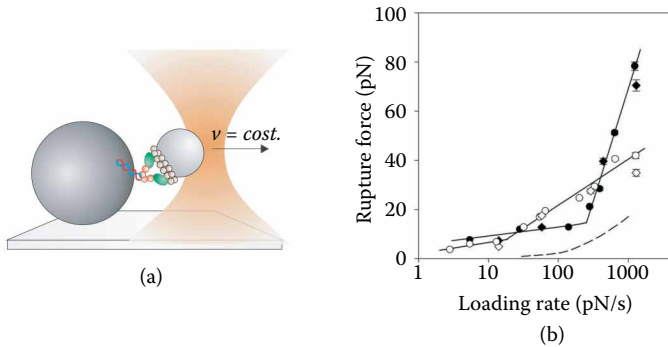
Figure 5.11 Dynamic force spectroscopy. (a) Cartoon representing dynamic force spectroscopy applied to actin–myosin bond. The molecular bond is subjected to constant loading rates and rupture forces and bond lifetimes are measured. (b) The characteristic rupture force of actomyosin bonds over a range of loading rates. At higher loading rates, actomyosin–ADP bonds (full circle) appear to be stronger than rigor bonds (empty circles). Corresponding data from single-headed HMM in each state (full and empty diamonds) are superimposed. The dashed line indicates the rigor behavior predicted from step-load data (From Guo, B., et al., *Proc Natl Acad Sci U S A*, 103, 9844–9849, 2006.). Error bars represent standard error of the mean (SEM).

and increasing the optical power at a constant rate ($dF_{trap}/dt = -(dk_{trap}/dt) \cdot x_{bead}$) (de Messieres et al. 2012). Data collected with DFS can be converted, using appropriate models, to get the kinetics of bond detachment under constant forces (Evans 2001; Dudko et al. 2008). Such an approach has been commonly used for weak bonds, in which the kinetics are too fast to effectively work in force-clamp geometries. However, a proper conversion relies on the accuracy of the model assumptions. Moreover, recently, alternative techniques such as ultrafast force-clamp spectroscopy opened the possibility to direct probing rapid force-dependent kinetics of molecular bonds, with unbinding rates on the order of several tens of kHz.

Among the many reports, DFS was applied to study the interaction between actin and skeletal muscle myosin (Guo and Guilford 2006; Lewalle et al. 2008) or titin (Bianco et al. 2007), and between lipid bilayers and myosin I (Pyrpassopoulos et al. 2010). The binding of the glycoprotein Ibα (GPIbα) subunit to the A1 domain of von Willebrand factor (VWF), which mediates the formation of platelet plugs for arterioles and is associated with the bleeding disorder von Willebrand disease, was recently studied by DFS (Arya et al. 2005; Kim et al. 2010).

5.4   Spatial Resolution

As described in the previous paragraphs, one of the key features of optical tweezers is the capability to measure conformational changes and displacements produced by single biological molecules. Such movements range from several

nanometers for cytoskeletal molecular motors, down to one base pair (~3.6 angstrom) for DNA and RNA processing enzymes (Greenleaf et al. 2007; Veigel and Schmidt 2011). High spatial resolution is, thus, a fundamental requirement for the study of a wide range of biological molecules. Molecular displacements can be measured through different position detection systems (Section 5.6.3). The most sensitive detectors to date, which are based on interferometry (Svoboda et al. 1993; Allersma et al. 1998; Gittes and Schmidt 1998c), allow detection of angstrom movements on a time scale of 1 ms or better. When properly optimized, position detectors do not set a lower limit on spatial and temporal resolution of optical tweezers. We showed in Section 5.2.2.2 that the movements of a bead trapped in optical tweezers are governed by Brownian fluctuations owing to thermal forces, which are inherent in single molecule experiments performed in liquid solution at ambient temperature. Thermal noise, indeed, sets fundamental limits on position and force measurements with single molecules.

5.4.1   Thermal Noise

Understanding which parameters affect thermal noise is crucial to optimizing spatial resolution in position measurements with optical tweezers. We have already showed that the amplitude and frequency distribution of thermal fluctuations of a trapped bead depend on the stiffness and viscosity of the system (Section 5.2.2.2). Here, we consider the single-bead geometry described in Section 5.3.1, in which the trapped bead is linked to a motor protein moving along its cytoskeletal filament, and we evaluate how to optimize the measurement of the motor step size. The system has a combined stiffness k, which comprises the trap stiffness (k_{trap}) and the stiffness of the molecule and the linkages connecting the molecule to the bead and to the coverslip surface (k_{motor}). The drag coefficient is mainly due to the bead, since the viscous drag of the motor protein is negligible with respect to that of a micrometer-sized bead (Figure 5.12a). The power spectrum of thermal motion is again given by Equation 5.11, where $\gamma = \gamma_{bead}$ and $k = k_{trap} + k_{motor}$ (both the optical trap and the motor protein are rigidly coupled to the ground, so that the two springs act in parallel and sum with each other, as represented in Figure 5.12b). The amplitude of thermal noise (position variance) is given by Equation 5.9. In an actual experiment, however, the bead position is always measured over a finite frequency interval or bandwidth Δf, owing, for example, to the cut-off frequency of the position detector, which sets a high frequency limit, and the limited time the motor protein spends in a fixed position, which sets a low frequency limit. In such a case, the position variance is the area under the power spectrum within the interval Δf (e.g., the turquoise area depicted in Figure 5.13). Therefore, an easy way to reduce the measured thermal noise is by shrinking the measurement bandwidth Δf. This can be achieved, for example, by simply filtering data with a moving time-average window. Such a procedure allows bringing bandwidth in the low-frequency regime ($f \ll f_C$) in which Equation 5.11 reduces to $S_x(f \ll f_C) = 4k_B T\gamma_{bead}/k^2$ and

$$\sigma_x = \sqrt{S_x(f \ll f_C) \cdot \Delta f} = \frac{\sqrt{4k_B T\gamma_{bead}\Delta f}}{k} \tag{5.13}$$

(a)

(b)
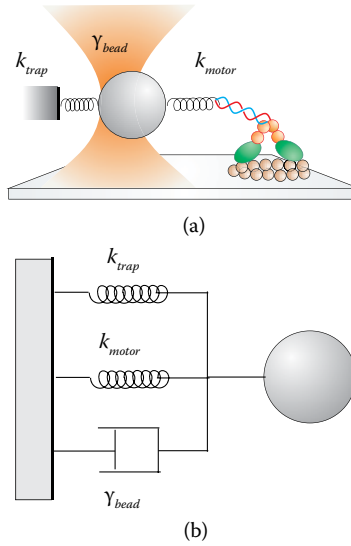
Figure 5.12 Mechanical elements affecting thermal noise in a single-bead assay. (a) k_{trap} is the trap stiffness and k_{motor} comprises the motor protein stiffness in series with the stiffness of the linkages connecting the protein to the bead and the coverslip surface. γ_{bead} is the bead viscous drag coefficient. (b) Mechanical model of the single-bead assay represented in (a); k_{trap}, k_{motor}, and the viscous drag γ_{bead} act in parallel on the microsphere.
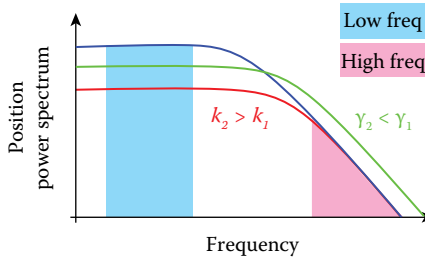
Figure 5.13 Power density spectrum of thermal noise of the bead position. When the stiffness of the system increases ($k_2 > k_1$), the noise amplitude decreases at low frequencies ($f \ll f_C$) (turquoise area), but it is unchanged at high frequencies (pink area). When the viscous drag decreases ($\gamma_2 < \gamma_1$), the low-frequency noise decreases, whereas the high-frequency noise increases. The area under the power spectrum stays constant.

Equation 5.13 tells us that, besides reducing measurement bandwidth, low position noise can be achieved by increasing system stiffness (large k) and using small beads (small γ_{bead}). In fact, the total amplitude of thermal noise is reduced when the bead is linked to a stiffer element (Figure 5.13, red curve). On the contrary, a smaller bead does not change the total amplitude of thermal motion (Equation 5.9 is

independent of γ) but changes its spectral distribution, leaving less noise at the low frequencies in which measurements are usually made (Figure 5.13, green curve).

The system stiffness can be increased either by using stiffer traps (increasing laser power) or by using stiffer molecules, or both. However, increasing trap stiffness has a zero net effect on the signal-to-noise ratio (SNR) of the measurement of molecular motor step size. In fact, combining Equations 5.12 and 5.13, the SNR is given by

$$\text{SNR} = \frac{x_{bead}}{\sigma_x} = \frac{k_{motor}x_{motor}}{\sqrt{4k_BT\gamma_{bead}\Delta f}} \tag{5.14}$$

We see from Equations 5.12 through 5.14 that increasing trap stiffness indeed reduces thermal noise, but it also reduces movements of the probe relative to the real movements of the molecule, so that the SNR is not changed. Equation 5.14 is still valid in case we are measuring motor step size using an ideal force clamp; in fact, since the optical force is kept constant ($dF_{trap} = -k_{trap}dx_{bead} = 0$), the thermal force is not influenced by the trap stiffness but only by the molecule stiffness; moreover, in a force clamp, the bead and trap movements are equal to the motor movement (Gittes and Schmidt 1998a).

Since high trap stiffness does not help in measuring steps of single molecular motors, researchers have worked on increasing the stiffness of biological constructs. This can be achieved by using functional truncations of the molecule under study (the stiffness of an elastic element decreases with its length [Howard 2001]), using rigid molecules to connect the protein under study to the bead and the coverslip surface (e.g., using biotin–avidin or covalent bonds), and by pretensioning the molecule. In fact, the stiffness of biological molecules is usually nonlinear and increases with the applied tension. However, even after pretensioning, typical protein stiffness does not exceed a few pN/nm.

Unfortunately, bead dimension also cannot be indefinitely reduced owing to a consequent reduction in optical tweezers force and sensitivity in position measurement (see Table 5.1 and Box 5.1), so that it is usually very difficult to work with microsphere diameters below 200 nm.

Similar conclusions can be drawn for the two-bead assay, in which a single molecule is tethered between two microbeads trapped in optical tweezers (Figure 5.7). However, trap and molecular stiffness sum up differently in this case. For example, with reference to Figure 5.14, the stiffness of the molecule (k_{DNA}) and the stiffness of the right trap (k_2) act in series, and this combined elastic element acts on the left bead in parallel with the left trap (k_1). This is analogous to the single bead described above, where the rigid attachment to the coverslip is replaced by the right bead trapped in optical tweezers. As a consequence, the added Brownian noise due to the second microsphere deteriorates the SNR, which now depends on the stiffness of the second trap (k_2) and is always smaller compared to the single-bead assay (Moffitt et al. 2006). However, Moffitt et al. demonstrated that by detecting the positions of both trapped microspheres ($x1_{bead}$ and $x2_{bead}$), correlations in their motions can be exploited to maximize the SNR. In fact, the difference coordinate ($x_d = x1_{bead} - x2_{bead}$), with appropriate choice of experimental parameters displays a SNR that is always superior to that of the single-trap geometry (Moffitt et al. 2006).

(a)

(b)
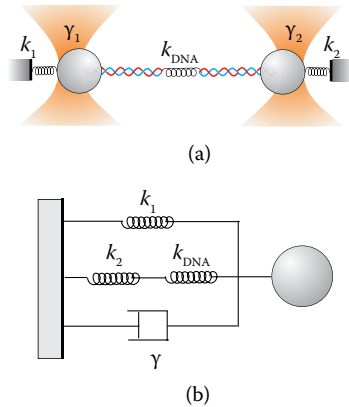
Figure 5.14 Mechanical elements affecting thermal noise in a two-bead assay. (a) k_1 and k_2 are the elastic constants of the two traps, k_{DNA} comprises the DNA stiffness in series with the stiffness of the linkages connecting the polymer to the beads. γ_1 and γ_2 are the viscous drag coefficients of the two beads. (b) Model of the mechanical elements acting on the left bead in the two-bead assay represented in (a); k_1 and the series of k_{DNA} and k_2 act in parallel on the left microsphere. The viscous drag γ depends on γ_1, γ_2, their hydrodynamic coupling, and the stiffness of the DNA molecule and traps (Moffitt et al. 2006). In case we neglect hydrodynamic coupling between the two beads, γ goes from γ_1 when $k_{DNA} \ll k_{1,2}$ (floppy dumbbell, the movement of the two beads is uncoupled) to $\gamma = \gamma_1 + \gamma_2$ for $k_{DNA} \gg k_{1,2}$ (rigid dumbbell, the movement of the two beads is perfectly coupled).

5.4.2　Instrumental Noise

Thermal fluctuations set a lower limit for high-resolution position measurements, but many sources of instrumental noise deteriorate spatial resolution in optical tweezers. Mechanical oscillations, acoustic noise, thermal expansion, and contraction of the microscope (thermal drifts), as well as laser pointing and intensity instabilities, all negatively affect position measurements. Therefore, high-resolution measurements in surface-coupled geometries (Figures 5.6 and 5.8) require stabilization of both the trapping laser and the microscope stage to reach spatial resolutions near the thermal noise limit. Both active and passive strategies have been adopted in the last decade to address this issue.

Active stabilization of the microscope stage is usually obtained through feedback systems that monitor movements of the stage using a fiducial mark attached to the coverslip surface and compensate such movements using piezo translators. Simple video microscopy can be used, as illustrated in Box 5.3, to monitor movements of a bead stuck to a microscope coverslip and compensate thermal drifts to less than 1 nm in three dimensions (Capitanio et al. 2005). On the contrary, nanometer stability of the trapping laser is achievable with a simple design to minimize air turbulence and laser intensity fluctuations, as described in Section 5.6.5 (Capitanio et al. 2005, 2007b; Monico et al. 2014). Steffen et al. developed such

a nanometer-stabilized system to reveal the distribution of binding sites of a single myosin molecule along an actin filament (Steffen et al. 2001).

A much more complex approach is required to reach angstrom stabilization, which is necessary to measure single base pair movements of nucleic acid processing enzymes. Carter et al. used a second laser source and back focal-plane interferometry to monitor the movements of a fiducial mark microfabricated onto the chamber surface and thereby correct thermal drifts using a piezo stage down to ~0.1 nm (Carter et al. 2007). Stabilization of the trapping laser was achieved using an optical fiber to convert laser pointing noise into intensity noise and actively stabilizing it with a feedback loop involving an acousto-optic modulator. Combining stabilization of the sample and the trapping laser, they demonstrated sensitivity to single base-pair steps in a surface-coupled DNA assay (Carter et al. 2007, 2009).

An alternative approach to active stabilization consists of decoupling the biological system under study from the coverslip surface by suspending it between two optical tweezers, formerly stabilized to the required accuracy level. Abbondanzieri et al. reduced laser pointing noise induced by air turbulence by enclosing the laser path within a closed chamber filled with a gas at low refractive index and temperature-stabilizing the experimental apparatus down to 0.1 K variation. They reported ~1 Å position noise when trapping a single bead ($R = 350$ nm) in a stiff trap ($k_{trap} = 1.9$ pN/nm) with a bandwidth $\Delta f = 100$ Hz. In those conditions, Equation 5.13 gives a thermal position noise of ~0.5 Å, close to that reported. By using this ultrastable optical trapping setup, they could probe single base-pair stepping by RNA polymerase (Figure 5.7c) (Abbondanzieri et al. 2005). Using similar double optical tweezers, Cheng et al. could measure single base-pair unwinding of double-stranded RNA by the hepatitis C virus NS3 helicase (Cheng et al. 2011). In this experiment, the setup was temperature stabilized, employed a low-noise laser (Cheng et al. 2010) and the differential detection described in the previous section (Moffitt et al. 2006).

In Section 5.6.5, we investigate the different sources of instrumental noise and give details on strategies that can be adopted to limit them.

5.5 Temporal Resolution

Optical tweezers are affected by various limitations in their capacity to temporally resolve events; the term *temporal resolution* can, thus, refer to different physical quantities and vary depending on the molecule under investigation. Position data can be sampled at high frequencies (hundreds of kilohertz), limited by the bandwidth of the photodetector and electronics. Temporal resolution of the position detector, however, is rarely the limiting factor in optical tweezers measurements.

5.5.1 Relaxation Time

A lower limit on temporal resolution of optical tweezers is given by the relaxation time of the system. In Section 5.2.2.1, we have shown that when a single bead trapped in optical tweezers is perturbed from equilibrium, for example, by protein conformational changes or by trap displacements, it moves exponentially to a new equilibrium position with a time constant (relaxation time) $\tau = \gamma/k$, where γ is the viscous drag coefficient and k the stiffness of the system ($\gamma = \gamma_{bead}$

and $k = k_{trap}$ in that example). Therefore, systems with high stiffness attached to small probes exhibit fast responses to perturbations. If the perturbation develops faster than τ, the bead moves with the same relaxation time τ, filtering out all the movements that occur on shorter time scales.

Let us consider again the arrangement depicted in Figure 5.6a, where a micrometer-sized bead is trapped in optical tweezers and linked to a biological molecule, immersed in a viscous solution. For such a surface-coupled geometry, the stiffness of the surface-coupled molecule and the stiffness of the optical tweezers act in parallel and sum with each other ($k = k_{trap} + k_{motor}$ in Figure 5.12). Therefore, beads attached to rigid molecules display fast temporal responses even in the presence of weak traps. In principle, relaxation times of ~2 μs can be reached with rigid molecules (1 pN/nm) using small beads (200 nm diameter), as shown in Table 5.2. Such values are, however, difficult to reach since, as previously observed in Section 5.4.1, high pretensioning is required to reach stiffness values on the order of 1 pN/nm. Moreover, the force exerted by optical tweezers and the resolution of the position detector both decrease with bead size, making the use of small beads difficult.

Several groups have worked on optimizing the relaxation time of optical tweezers to study biological molecules with high temporal resolution. Nishiyama et al. developed a dark-field position detection scheme with increased signal-to-noise ratio that allowed them to effectively use 200 nm diameter beads in an optical trap. By applying tension to a single kinesin motor proceeding along a microtubule to increase its stiffness, they obtained a response time $\tau < 20$ μs at forces above 3 pN. The high temporal resolution allowed them to detect 4 nm substeps within the 8 nm step of kinesin (Nishiyama et al. 2001). Uemura et al. used the same assay to study the stepping of myosin Va at high spatiotemporal resolution, revealing two pathways for the 36 nm steps, one of them composed by 12 and 24 nm substeps (Uemura et al. 2004). A modified setup was used by Iwaki et al. to tether a single-headed myosin VI to an optically trapped 200 nm bead and rapidly scan the bead along an actin filament (Iwaki et al. 2009). Using this assay, they could observe weak and strong binding of myosin VI heads to actin, and they found that strong binding was greatly enhanced when backward strain was applied.

As observed in Section 5.4.1, trap and molecular stiffness sum up differently in the two-bead assay because of its uncoupling from the coverslip surface. With reference to Figure 5.14, the combined stiffness acting on the left bead is here given by $k = k_1 + \dfrac{k_2 k_{DNA}}{k_2 + k_{DNA}}$. The stiffness k is always smaller than the combined stiffness of the traps ($k_1 + k_2$) and reaches this limit only for very rigid molecules ($k_{DNA} \gg k_2$). Therefore, the relaxation time in this assay is dictated by the stiffness of the two traps, and high trap stiffness helps in both reducing thermal noise and increasing temporal resolution.

5.5.2 Compromise between Spatial and Temporal Resolution—Dead Time

The relaxation time constitutes a lower limit to time resolution that restricts the observable dynamics of biomolecules in optical tweezers. However, thermal fluctuations usually pose a more severe limitation on the time resolution

for event detection. In fact, as discussed in Section 5.4.1, to distinguish single base-pair steps with sufficient signal-to-noise ratio, a sufficiently small bandwidth has to be chosen to reduce thermal noise (Equation 5.13). A compromise between spatial and temporal resolution is thus necessary. Therefore, the capacity to detect and measure sub-nm displacements from single molecules requires averaging over several hundreds of milliseconds, thus reducing measurement bandwidth and temporal resolution. The limited temporal resolution sets a lower limit for the briefest detectable event (a molecular motor step in the previous example), which is called the *dead time*. Conformational changes of motor proteins occurring faster than the dead time are not detectable. Equation 5.14 gives the SNR for step detection in a single-bead geometry and can be generalized to a two-bead geometry as in Moffitt et al. (2006). Moffit et al. also gave an explicit expression for the inverse relationship between spatial resolution and temporal resolution (dead time) in a two-bead assay (Moffitt et al. 2008).

The above considerations apply when measuring steps of processive molecular motors and conformational changes or folding trajectories of single molecules in a single- or two-bead assay. A similar analysis can be done when investigating proteins that interact weakly with their binding partners in a three-bead assay, such as nonprocessive motors interacting with their cytoskeletal filament or transcription factors interacting with nonspecific DNA sequences during their target search. Such interactions are characterized by short interaction lifetimes: for example, nonprocessive motors bind to their filament for just one ATP cycle, which lasts for a few milliseconds under physiological conditions. The dead time for the detection of these short interactions is strictly related to the detection method used.

Methods for the detection of interactions of nonprocessive motors in the three-bead assay were first developed in studies on muscle myosin (Figure 5.8a). As briefly introduced in Section 5.3.3, the detection strategy was based on the variation of thermal noise upon binding, which, in turn, depends on the variation of system stiffness, as described by Equation 5.13 in the low-frequency region ($f \ll f_c$) (Molloy et al. 1995; Knight et al. 2001; Smith et al. 2001a). When myosin binds to actin, the system stiffness increases, and thermal fluctuations at low frequencies consequently decrease (as represented by the turquoise area under the blue and red power spectra in Figure 5.13). The ratio between thermal noise in the unbound and bound states $\sigma_u/\sigma_b = k_b/k_u$, where the subscripts u and b respectively indicate quantities measured in the unbound and bound states, can be as high as ~25 by using weak traps and by high pretensioning of the actin filament ($k_u \sim k_1 + k_2 \sim 0.04$ pN/nm; $k_b \sim k_m \sim 1$pN/nm) (see Figure 5.15) (Smith et al. 2001a; Capitanio et al. 2006).

In those experiments, the variance of thermal noise is calculated from position data using a time-window consisting of W data points. The signal used to separate bound from unbound events is given by the distance between the variance of the two states $\sigma_u^2 - \sigma_b^2$, while the noise is given by the sum of the standard deviations of those variance states:

$$\text{SNR} = \frac{\sigma_u^2 - \sigma_b^2}{\sigma\left(\sigma_u^2\right) + \sigma\left(\sigma_b^2\right)} \sim \sqrt{\frac{W}{2}}\, \frac{\sigma_u^2 - \sigma_b^2}{\sigma_u^2 + \sigma_b^2} \sim \sqrt{\frac{W}{2}}\, \frac{k_b^2 - k_u^2}{k_b^2 + k_u^2} \tag{5.15}$$

(a)

(b)
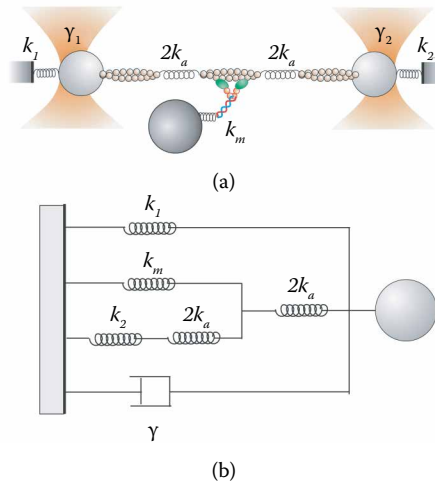
Figure 5.15 Mechanical elements in a three-bead assay. (a) k_1 and k_2 are the elastic constants of the two traps, $2k_a$ is the stiffness of half actin filament in series with the stiffness of one linkage connecting actin to one of the two beads, k_m the stiffness of the myosin molecule, which binds in the middle of the actin filament. γ_1 and γ_2 are the viscous drag coefficients of the two beads. (b) Model of the mechanical elements acting on the left bead in the three-bead assay represented in (a); the left bead is connected to the left trap k_1 and to half of the actin filament $2k_a$, which is connected in series with the parallel of the myosin molecule k_m and the other half of actin $2k_a$ in series with the left microsphere k_2. The viscous drag γ depends on γ_1, γ_2, their hydrodynamic coupling, and the stiffness of all the elastic elements (Smith 1998; Moffitt et al. 2006). In case we neglect hydrodynamic coupling between the two beads, γ goes from γ_1 when $k_a \ll k_{1,2}$ (floppy dumbbell, the movement of the two beads is uncoupled) to $\gamma = \gamma_1 + \gamma_2$ for $k_a \gg k_{1,2}$, k_m (rigid dumbbell, the movement of the two beads is perfectly coupled). When myosin detaches from actin, the model is still valid with $k_m = 0$.

The first approximation in Equation 5.15 is obtained for $W \gg 1$ (Smith et al. 2001a), while the second is for $f \ll fc$. Although sufficiently high SNR can be obtained for $W > 50$, if the acquisition rate of data points is too high, the above approximation is no longer valid. In fact, $\sigma_u^2 - \sigma_b^2$ and the SNR progressively decrease with frequency, from the value given by Equation 5.15 for $f \ll fc$ down to 0 when the position variance is measured at $f \gg f_c$ (as represented by the pink area in Figure 5.13, which is the same for the blue and red power spectra). For this reason, position variance in this kind of experiment must be calculated using time windows $\Delta t > 5$ ms (Smith et al. 2001a), and events with durations below this value are not detectable. Δt is, thus, the dead time for detection of molecular interactions in a conventional three-bead assay.

Different approaches have been recently developed to overcome such limitation. Veigel et al. developed a technique to decrease the dead time in a three-bead

geometry to about 1 ms (Veigel et al. 1999). The idea was to artificially increase the position noise (and thus the signal in Equation 5.15) at a high frequency by oscillating one trap at 1 KHz and detecting the amplitude of oscillation at the other bead, which was greatly reduced upon myosin binding. This method enabled them to detect the onset of each binding event within ~1–2 ms.

An additional complication of the three-bead assay is that it is an unloaded configuration, in which the actin filament is in equilibrium, with the two traps applying equal and opposing forces that sum up to zero. Application of loads in this assay requires putting the system out of equilibrium, for example, by moving the traps after detection of actin–myosin attachment. Such a procedure introduces a *time lag* between myosin attachment and application of the force that is again limited by the dead time (Veigel et al. 2003). Veigel et al. were able to apply a range of loads to a single myosin head with a time lag of ~4–5 ms, which allowed them to investigate the effects of load on the kinetics of the second step of smooth muscle myosin (Veigel et al. 2003) and myosin Va (Veigel et al. 2005). These experiments made a great contribution to the current understanding of how load regulates myosin motors function and how it plays a role in coordination of the two motor domains in processive motors. The several milliseconds lag of this technique, however, did not allow the study of load dependence of faster processes, such as the first step in myosin working stroke. Moreover, techniques capable of clamping force on non-processive motors and weak molecular bonds were still lacking.

5.5.3 Ultrafast Force-Clamp Spectroscopy

A different approach, named *ultrafast force-clamp spectroscopy*, allows application of constant loads between a single intermittently interacting biological polymer and a binding protein with a time lag in the application of load that is only limited by the relaxation time of the system, and with a much improved dead time for interaction detection (Capitanio et al. 2012).

A sketch of the operational principle of the method is shown in Figure 5.16a, in which A is the binding protein, and B is the polymer. A net constant force ($F_{tot} = +\Delta F$) is applied to the bead–polymer–bead complex (dumbbell) through two feedback systems that clamp the force on the two beads to two different values ($-F$ on the left bead and $F+\Delta F$ on the right bead). The dumbbell, thus, moves against viscous drag at constant velocity ($v_u = F_{tot}/\gamma$) when molecules A and B are not bound. The net force is alternated in direction, so that the dumbbell oscillates in a triangular wave fashion within a limited spatial interval (Figure 5.16b). When A binds to B, the force F_{tot} is transferred to the surface-coupled molecule A. The system dynamics is analogous to that described in Section 5.2.2.1 and Equation 5.8, in which a constant force is applied to A and the system exponentially reaches an equilibrium position and stops ($v_b = 0$).

The time taken to transfer the force from the viscous solution to molecule A and stop the dumbbell is the relaxation time of the molecular complex, which also represents the time lag for force application. When applied to the interaction between fast skeletal muscle myosin and actin using highly pretensioned actin filaments and 500 nm diameter beads, the time lag can be as short as ~10 μs (see Table 5.2). For lactose repressor interactions with a weakly tensioned DNA
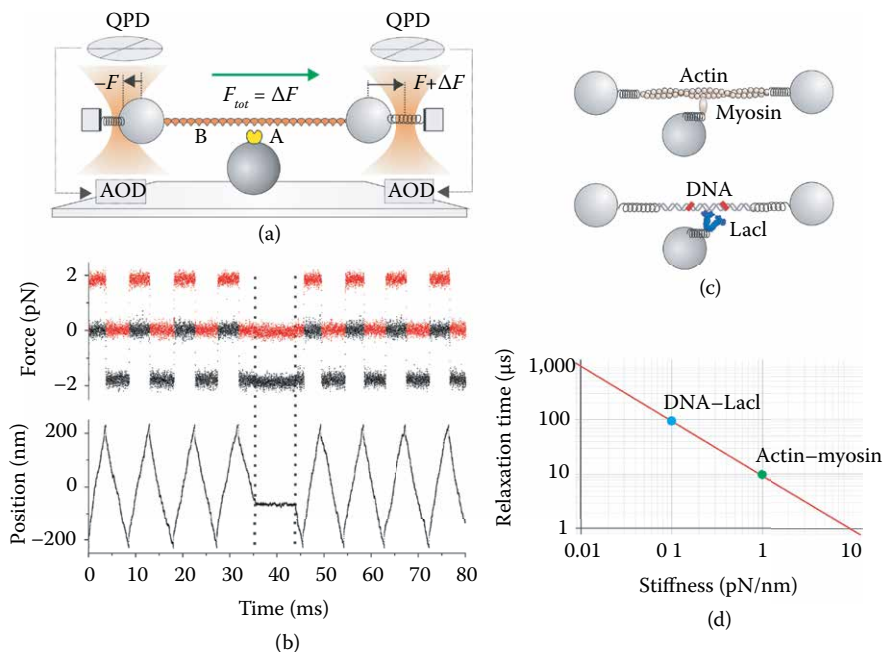
Figure 5.16 Ultrafast force-clamp spectroscopy. (a) The operational principle of the method illustrating constant force $F_{tot} = \Delta F$ applied to the polymer B through two feedback systems clamping the force on the left bead to F and on the right bead to $F + \Delta F$. The force is measured using quadrant detector photodiodes and kept constant by moving the traps via AODs. (b) *Top*: ΔF on left (black) and right (red) beads. *Bottom*: Position of one of the two traps. The force is switched between $+\Delta F$ and $-\Delta F$ to keep the dumbbell within a confined spatial interval (± 200 nm). The dumbbell stops when A binds to B (dotted lines). (c) Mechanical model for actin–myosin and DNA-LacI interaction. (d) Relaxation times versus stiffness calculated from the models in panel (c) using 500 nm diameter beads.

($\sim$3 pN), which is characterized by a $\sim$10 times smaller stiffness, the lag is $\sim$100 μs (Figure 5.16c and d). These time lags are very short compared with the duration of typical protein interactions, which, thus, occur under a real force-clamp configuration. Any conformational change occurring after the formation of the molecular bond is also performed under the same constant load (Figure 5.17). Using this system, we could directly apply constant loads before the onset of the first step of myosin and directly measure load dependence of the amplitude of myosin working stroke (Capitanio et al. 2012).

Another advantage of this system is the short dead time. Here, interactions are detected from variations in the dumbbell velocity, which occur with the same short relaxation time of the system, rather than through variations in position noise, which have to be evaluated on a time scale much longer than the relaxation time to give a detectable signal, as discussed in the previous paragraph.
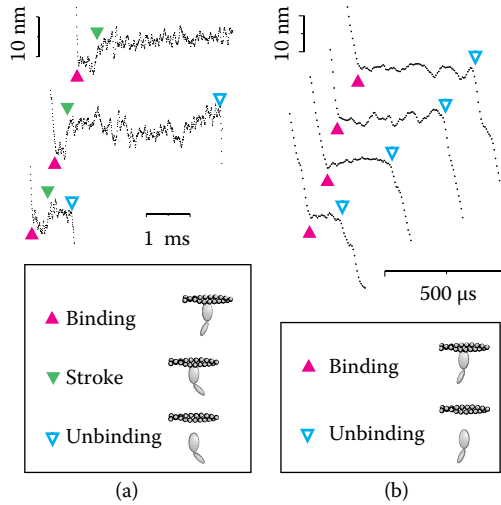
Figure 5.17 Typical interactions in ultrafast force-clamp spectroscopy. (a) Actin-myosin interactions longer than 1 ms showed that the myosin working stroke is developed 0.2–1 ms after attachment. (b) Submillisecond single actin–myosin interactions detected with ultrafast force-clamp spectroscopy. (Filled arrowheads pointing up: Actin–myosin binding. Filled arrowheads pointing down: Myosin working stroke. Open arrowheads pointing down: Actin–myosin detachment).

Therefore, the variation of velocity upon binding ($v_u - v_b = F_{tot}/\gamma$) displays a high signal-to-noise ratio on time scales close to the relaxation time, especially for small beads and high forces. High values of molecular stiffness also increase SNR by reducing thermal noise. For example, the dead time for a rigid actin–myosin dumbbell is ~100 μs at ~5 pN, using 500 nm diameter beads, which allowed the detection of weak actin–myosin interactions (detachment ~5×10^3 s^{-1} at 5 pN), and premature detachment of myosin from actin (~1×10^3 s^{-1} at 5 pN). On Lac repressor interacting with a weakly tensioned DNA, sub–ms interactions are still clearly detectable, allowing the detection of short-lived interactions (dissociating at ~1×10^3 s^{-1} at 4 pN) that are probably involved in Lac repressor facilitated diffusion mechanism (Berg et al. 1981; Monico et al. 2013).

5.5.4 Ensemble Averages

Ensemble averaging is a useful technique when high spatial and temporal resolutions are both required (Veigel et al. 1999; Veigel et al. 2002; Chen et al. 2012). This method enabled distinguishing two steps in the working stroke of myosin Va (Veigel et al. 2002), smooth muscle myosin (Veigel et al. 2003), and skeletal muscle myosin (Capitanio et al. 2006), and excluded the presence of substeps in kinesin (Carter and Cross 2005) (Figure 5.18). Instead of time-averaging position data of single events to reduce thermal noise, as prescribed by Equation 5.13, in ensemble averaging, N interaction events are synchronized at the beginning or at the end of the interaction and averaged point-by-point. Position noise thus scales as $1/\sqrt{N}$
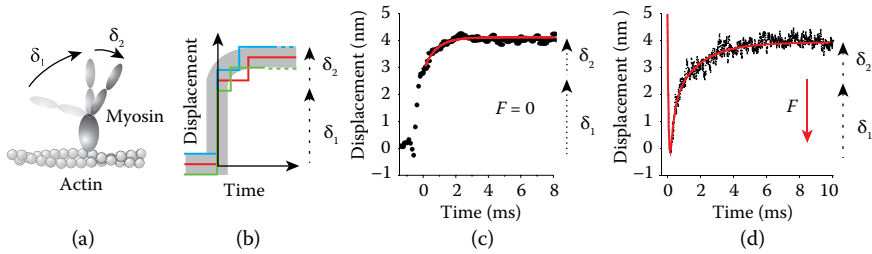
Figure 5.18 Ensemble averages. (a) Myosin working stroke is made of two steps (δ1, δ2). (b) Single actin–myosin interactions (continuous green, red, and blue lines) are composed by two subsequent steps. In ensemble averages, interactions are aligned at their beginning (forward average) or end (backward average, not shown). In the forward average, the last position value of each event is replicated (dotted lines) to match the length of the longest event (red). Ensemble averages (gray lines) are obtained by averaging the events point by point. (c) Ensemble average analysis of interactions between actin and fast skeletal myosin acquired with an unloaded three-bead assay evidenced that a first step (~3.5 nm) occurred very rapidly after myosin binding and was followed by a smaller step (~1 nm) in the same direction (Capitanio et al. 2006). The rate of development of the second step is obtained by fitting the rising phase of the second step with an exponential function (red curve). (d) Ensemble average analysis of interactions between actin and fast skeletal myosin acquired with ultrafast force-clamp spectroscopy confirms that a rapid first step (~4 nm) was followed by a smaller step (~1 nm) (Capitanio et al. 2012). Force is 3.2 pN opposing the working stroke for the data reported in the figure. The increased temporal resolution allows fitting both steps with a double exponential function to obtain their rate of development (red curve).

and can reach the angstrom level for $N \sim 1000$ (Capitanio et al. 2006). Temporal resolution for this kind of average is determined by the accuracy in detecting the time of the beginning or end of the interaction (σ_A). Such accuracy has been evaluated through simulated data (Carter and Cross 2005; Capitanio et al. 2006) or theoretical considerations (Capitanio et al. 2012). For the interaction between fast skeletal muscle myosin and actin, $\sigma_A \sim 300$ μs can be obtained using an unloaded three-bead assay (Capitanio et al. 2006) and in the range 10–50 μs with ultrafast force-clamp spectroscopy (Capitanio et al. 2012). Methods have been developed to interpret the kinetics after an ensemble average and extract the rate constants of the different reactions within a biochemical cycle (Chen et al. 2012).

5.6   Optical Tweezers Setup

Optical tweezers are commonly introduced in a commercial microscope adapted to allow superimposition of the trapping laser with the microscope imaging path. However, optical tweezers can be also built together with the optical microscope as a custom setup. Both approaches have their own advantages and drawbacks.

Commercial microscopes are user friendly and easily allow interfacing with commercial software for image acquisition and device control. Lenses and optics are usually not optimized for their use with near-infrared light as commonly used in optical tweezers for biological applications. The mechanical structure sometimes shows insufficient mechanical stability for measuring nanometer or subnanometer protein conformational changes (see Section 5.4.2) and might be difficult to adapt to optical tweezers operation. Custom setups offer maximum freedom in design but cannot provide the same ease of operation of a commercial microscope. A third option is commercial optical tweezers setups. Among the others, you can find the Nanotracker 2 from JPK Instruments (www.jpk.com) and the C-trap and SuperC-trap from Lumicks (www.lumicks.com). For the price that you pay, you get years of development of optimized hardware and software to control the traps and analyze measurements as well as combined confocal or superresolution microscopy.

Whatever the choice, the basic components are always the same. Following, we give an overview of the instrumentation and optics composing an optical tweezers setup, with a particular focus on describing the basic concepts in optical tweezers design and important features for high-resolution single molecule measurements. Further technical details can be found in several reviews describing optical tweezers design (Fallman and Axner 1997; Smith et al. 1999; Neuman and Block 2004; Dienerowitz et al. 2008).

Figure 5.19 shows a sketch of a typical basic optical tweezers setup. The right-end side of the figure shows the optical microscope pathway, with brightfield illumination and imaging on the lower and upper ends, respectively, fluorescence excitation and detection, and the sample (S) between the objective (O) and the condenser (C). Optical tweezers are represented on the left side, with the trapping laser, beam expansion, and steering optics on the upper part, and position detection on the lower side.

5.6.1 Laser Source and Trapping Beam

When optical tweezers are used to manipulate biological samples, the trapping laser is usually chosen in the near-infrared region of the light spectrum. In fact, absorption of laser light and photodamage has been evaluated in previous works, and few wavelengths in the near-infrared region were found to minimize such effects (Neuman et al. 1999). A 1064 nm wavelength is commonly used because of the availability of high-power solid-state Nd:YAG lasers, even though it is about a factor of 2 more destructive than 830 and 970 nm light, where photodamage exhibits minima. Currently, single-mode diode lasers are available at all the favorable wavelengths, but only at relatively low power. We would like to point out, however, that photodamage is particularly important when working with live cells, whereas, for the purpose of single molecule *in vitro* studies, it is a less important concern. Since the laser source should exhibit high power, good pointing stability, low intensity noise, and high-quality TEM00 spatial mode, solid-state Nd:YAG lasers are still the best option for *in vitro* experiments.

Several optics are introduced in the beam path between the laser source and the microscope objective for optimal optical tweezers operation. With reference to Figure 5.19, after collimation by telescope T1, the laser beam typically
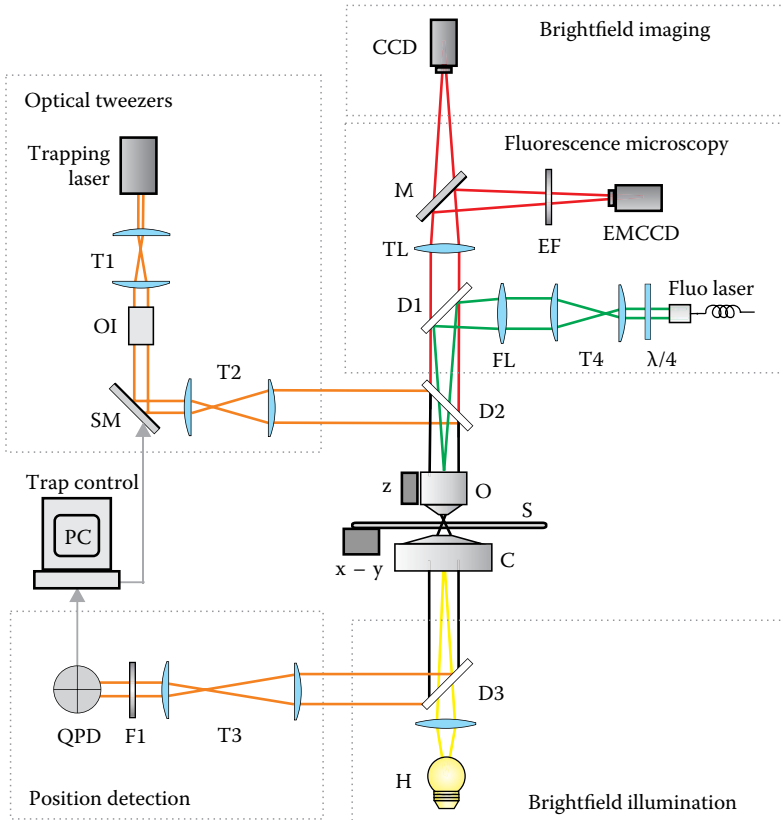
Figure 5.19 An optical tweezers setup. Brightfield illumination for the optical microscope (yellow line) is provided by a halogen lamp (H) and focused in the back focal plane of the condenser (C). The sample (S) can be translated and focused with piezo translators (*x-y* and *z*). The objective (O) and the tube lens (TL) project the image of the sample (black and red lines) on a CCD camera (CCD). Optical tweezers (orange line) are inserted and extracted from the optical axis of the microscope through dichroic mirrors (D2 and D3). The trapping beam is collimated by the telescope T1, passes through an optical isolator (OI), and is steered by a steering mirror (SM) controlled by a computer. The beam is expanded by the telescope T2 to match the dimension of the objective pupil. After the condenser, the dimension of the trapping beam is adapted to the quadrant photodiode detector (QPD) through a telescope T3 and filtered by an interference filter F1 to remove unwanted wavelengths. Signals from the QPD are acquired by a computer. Fluorescence excitation is provided by a laser (green line), circularly polarized by a $\lambda/4$ waveplate, expanded by the telescope T4, and focused on the back aperture of the objective through a focusing lens (FL). A dichroic mirror D1 separates excitation and emission wavelengths, and a movable mirror (M) allows switching between brightfield and fluorescence imaging, which is provided by an electron multiplied camera (EM CCD) after passing through the emission filter (EF).

passes through an optical isolator (OI). Such a device is important to avoid back-reflections of the beam inside the laser cavity, which otherwise cause large random amplitude fluctuations in the laser source.

Since trapping forces originate from the interaction of the dielectric particle and the gradient of light intensity, higher gradient results in higher trapping efficiency. Therefore, the beam dimensions must be adapted to slightly overfill the objective aperture. This allows the operator to fully exploit the objective numerical aperture to achieve maximum beam focusing and light intensity gradient. A second telescope is thus introduced in the optical path for this purpose (T2). For the same reason, the laser source must show a high-quality Gaussian TEM00 mode (i.e., a M quality factor close to 1) to get the smallest waist when focused by the microscope objective.

5.6.2   Beam Steering and Sample Movement

An important feature for optical tweezers is the capability of precisely moving the trap within the sample plane. This can be achieved by steering the laser beam by using a motorized mirror, an acousto-optic deflector, or an electro-optic deflector. The steering device must be precisely positioned in the beam path in order to convert beam angular deflections (ϑ) into trap movements in the sample plane (x). Figure 5.20 illustrates how this conversion is achieved.

The steering device is positioned in the back focal plane (BFP) of the first lens of the telescope T2 and the objective BFP is positioned in the forward focal plane (FFP) of the second lens of T2. Therefore, beam steering occurs on a plane conjugated to the objective BFP (blue dotted lines in Figure 5.20 represent conjugated planes), and rotation of the beam in the objective BFP is converted into trap displacement (x) in the sample plane by the objective lens. Since the objective BFP coincides with the objective back aperture, the beam remains centered on the aperture, independent of ϑ. Thus, proper optics alignment is important to avoid decentering and cutting part of the trapping beam at the objective aperture when the beam is rotated by the steering device.

Important features of the steering device are the maximum and minimum angular deflections (ϑ_{max} and ϑ_{min}) and angular stability (σ_ϑ), which, respectively, determine the maximum and minimum trap displacement (x_{max} and x_{min}) and its pointing stability (σ_x). Using geometrical optics approximation, we obtain the trap displacement at the sample plane (x) as a function of ϑ, the focal length of the objective (f_O), and the focal lengths of the telescope (f_1, f_2):

$$x \sim f_O \frac{f_1}{f_2}\vartheta = \frac{f_O}{M}\vartheta, \tag{5.16}$$

where $M = f_2/f_1$ is the magnification of telescope T2. Equation 5.16 relates x_{max}, x_{min}, and σ_x to ϑ_{max}, ϑ_{min}, and σ_ϑ, respectively, and guides us in the choice of a proper steering device given our experimental needs in terms of displacement and stability of the trap in the sample plane. Equation 5.16 also shows that large telescope magnification after the steering device (M) reduces the maximum displacement of the trap in the sample plane; at the same time, it allows smaller
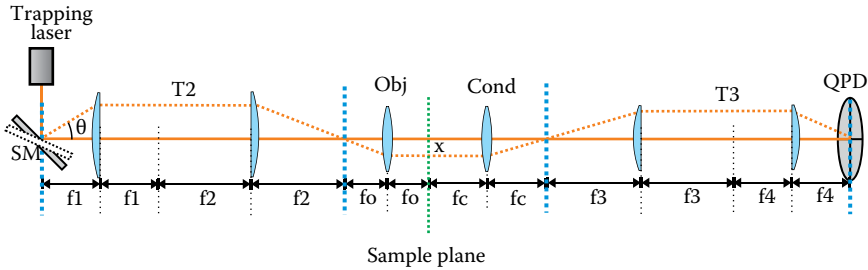
Figure 5.20 Optical path of the trapping beam. Beam steering propagates along the trapping laser path. Dotted blue lines indicate conjugated planes. When the beam direction is rotated by an angle θ by the steering mirror, the beam rotates at the back focal plane of the objective, which converts the rotation into beam translation *x* at the sample plane. Beam rotation also occurs at the condenser back focal plane and on the QPD.

minimum trap movements and reduces pointing noise. Therefore, the choice of proper magnification of the two telescopes T1 and T2 must take into account, on one hand, the required beam dimension at the objective back aperture and, on the other hand, experimental needs in terms of max/min trap displacements and pointing stability.

Another fundamental feature of the steering device is its deflection speed. Our needs in terms of speed depend again on the experimental configuration, as described in detail in Section 5.3. Electro-optic deflectors offer maximum speed and pointing stability, but limited angular deflection (Valentine et al. 2008). Acousto-optic devices are more commonly used. When driven with stable direct digital synthesizers (DDS) they offer angstrom movements and stability, large trap movements (~50 μm), and fast steering (few μs). Piezo-mirrors or mirrors driven by stepping motors offer larger deflections but with a much slower time response on the millisecond time scale, dictated by the inertia of mechanical movements.

5.6.3   Position Detection

Several position detection methods have been developed during the last decades (Neuman and Block 2004). Here we describe position detection with a quadrant photodiode (QPD) in the back focal plane of the condenser. This system is largely used owing to the high temporal and spatial resolution and capability of 2D and 3D position detection.

In this detection technique, the same laser source is usually used for both trapping and position detection. The trapping laser light, after being focused by the objective in the sample plane, is collected by the condenser and projected onto a QPD, which is positioned in a plane conjugated to the condenser BFP (Figure 5.20). The telescope T3 serves for both creating the conjugated plane and adapting the laser beam to the QPD size. In this configuration, the QPD images the far-field interference between light scattered by the trapped particle and unscattered light (Allersma et al. 1998; Gittes and Schmidt 1998c). The intensity

distribution of the interference pattern depends on the position of the bead rela-
tive to the trap and the intensity center-of-mass can be measured from differen-
tial voltage signals V_x and V_y obtained from the four quadrants currents i_A, i_B, i_C,
and i_D, and an operator circuit with gain g (Figure 5.21):

$$V_x = g\frac{(i_B + i_D) - (i_A + i_C)}{i_A + i_B + i_C + i_D}; \quad V_y = g\frac{(i_A + i_B) - (i_C + i_D)}{i_A + i_B + i_C + i_D}; \tag{5.17}$$

These voltage signals are linearly dependent on the bead displacement in the
usual range of optical tweezers operation, as discussed in Boxes 5.1 and 5.2.
Moreover, the axial position of the bead can be measured from the total light
intensity in the back focal plane of the condenser. Also the axial position signal
derives from the interference between the light scattered by the trapped particle
and unscattered light, as shown by Pralle et al. (Pralle et al. 1999).
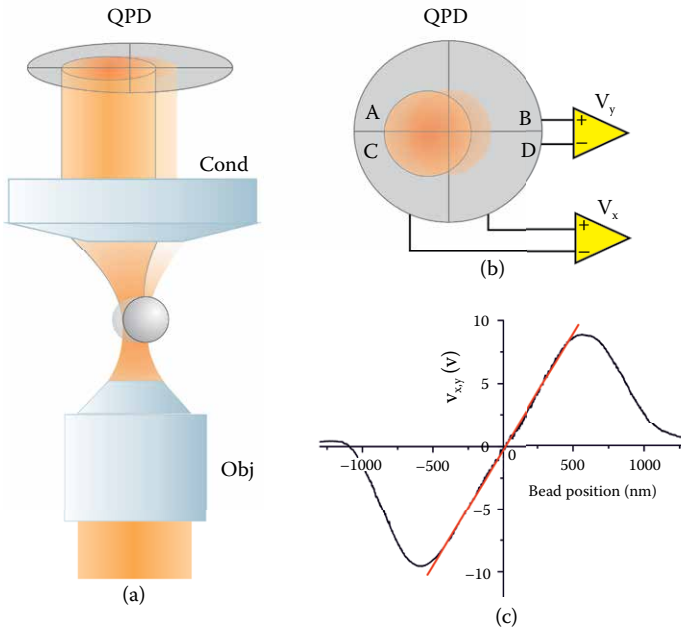
Figure 5.21 Position detection with a QPD positioned in the back focal plane of
the condenser. (a) When the bead is located in the center of the trap, the beam is
projected in the center of the QPD. As the bead is displaced laterally, the inten-
sity pattern on the QPD moves proportionally. (b) Position signals V_x and V_y are
obtained from differential amplifiers. (c) Position signals are proportional to the
bead displacement in a range of about ±500 nm from the trap center when using
1 micron diameter beads.

Box 5.2 Multiple Optical Tweezers

Multiple optical tweezers are very useful to manipulate multiple molecules simultaneously, stretch biological polymers, or apply tension on living cells. We previously discussed how double optical tweezers are used in a two- or three-bead configuration to investigate DNA elasticity, DNA processing enzymes, or molecular motors interacting with their cytoskeletal filament. Multiple optical tweezers (MOTs) can be obtained using different methods, but all of them are produced using either time-shared (TS) or continuous (CW) laser beams. The first class of MOT is obtained by rapidly moving a single optical trap between different positions in the sample plane; if the time taken to scan the different trap positions is much smaller than the diffusion time of the trapped particles, the laser beam works as stable multiple optical tweezers (Figure 5.22b). Faster scans imply that more traps can be generated simultaneously and/or that more efficient trapping can be achieved. TS traps
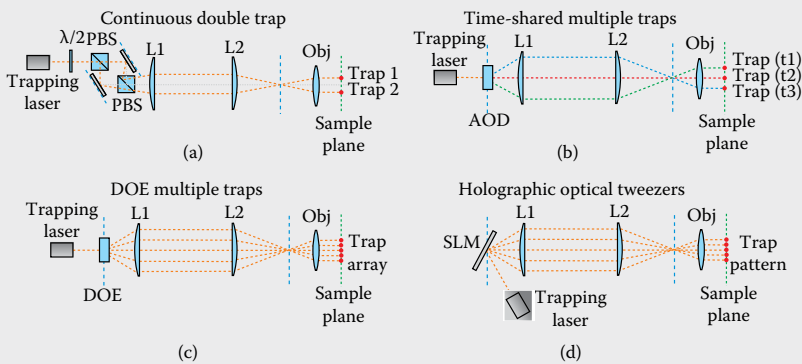
Figure 5.22 Configurations for multiple optical tweezers. (a) Continuous double trap. A single laser beam is split by a polarizing beam-splitter cube (PBS). A $\lambda/2$ waveplate allows regulating the laser power in the two arms. Two mirrors, in planes conjugated to the objective back focal plane, rotate the beams, which are then overlapped by a second PBS. The rotation is converted by the objective lens into trap movements in the sample plane. (b) Time-shared multiple traps. An acousto-optic deflector (AOD) rapidly steers the laser beam in multiple angles, which are converted by the objective lens into multiple trap positions in the sample plane. (c) Diffractive optic multiple traps. A diffractive optic placed in a plane conjugated to the objective back focal plane produce an array of laser beam at different angles, which correspond to an array of spots in the sample plane. (d) Holographic optical tweezers. A spatial light modulator (SLM) placed in a plane conjugated to the objective back focal plane produces a pattern of laser beam at different angles, which corresponds to an array of spots in the sample plane.

have been obtained by deflecting the laser beam using piezoelectric mirrors (Mio et al. 2000), galvano mirrors (Sasaki et al. 1991), or acousto-optic deflectors (AODs) (Visscher et al. 1996; Nambiar and Meiners 2002; Guilford et al. 2004; Noom et al. 2007). Depending on the technique used, scanning rates can reach, respectively, 1–2, 10–50, and 10–200 kHz. The generation of the traps is usually controlled from a computer, so that the number of traps, their position, and stiffness can all be modified in real time. TS tweezers are easily built and aligned, since only one laser beam is needed.

CW MOT are obtained by simply dividing a beam into two or more optical paths and then recombining the beams before the objective (Finer et al. 1994); alternatively, two or more laser sources can be combined together (Visscher et al. 1996). This approach is simple when only two traps are needed (Figure 5.22a), but becomes more complicated when multiple traps are required. In those cases, diffractive optical elements or computer-generated holograms can be used to obtain static trap arrays (Figure 5.22c) (Dufresne and Grier 1998; Dufresne et al. 2001), or spatial light modulators that allow real-time control of trap positions in the sample volume (Figure 5.22d) (Liesener et al. 2000; Curtis et al. 2002; Grier 2003).

The double optical tweezers used in the two- and three-bead assays described in Section 5.3 are usually realized by splitting a single laser beam with polarizing beam splitters, resulting in two continuous laser beams (Figure 5.22a). An alternative approach consists in time-sharing the laser beam between the two traps by rapidly moving it between the two positions using AODs (Guilford et al. 2004). Recently, such an approach has been used to build a high-resolution optical trap combined with single-fluorophore sensitivity (see Section 5.7.1) (Comstock et al. 2011). A drawback of the time-shared double trap is that the dumbbell oscillates because of the alternate presence of just one trap that pulls toward it (Capitanio et al. 2007a). The amplitude of the oscillation depends on the relaxation time of the dumbbell in the traps ($\tau \sim 2\gamma_{bead}/2k_{trap}$ for a rigid dumbbell), on the commutation time of the traps, and on the tension imposed to the filament, and usually ranges from ~1 nm at 100 kHz commutation time (close to the limit of AODs) to ~10–20 nm at 10 kHz commutation time. Therefore, the position detection strategy must take into account such oscillations to attain the few-Armstrongs accuracy as reported by Comstock et al.

The signal-to-noise ratio in lateral position detection is maximized when the numerical aperture of the detector is maximized, contrary to axial position detection, which is inversely proportional to the numerical aperture.

5.6.4 Combining Fluorescence Microscopy

The combination of optical tweezers with fluorescence microscopy is very useful whenever a need to visualize the molecules under study or to acquire

simultaneous fluorescence and mechanical data emerges. Different illumination schemes for fluorescence microscopy have been adopted depending on the biological application, as described in Section 5.7.2. Here, we briefly illustrate simple wide-field illumination, as schematically depicted in Figure 5.19. Illumination for fluorescence microscopy is usually supplied by one or more laser sources, which provide the high power that is necessary to get detectable signals from single chromophores. Since the laser light is usually linearly polarized, the light polarization must be circularized by a λ/4 waveplate to maximize excitation of single chromophores, independent of their orientation in the sample plane. The beam is then magnified using a telescope (T4) and focused by a lens (FL) in the back focal plane of the objective to get a collimated beam on the sample plane with uniform intensity within the field of view. A long-pass dichroic mirror (D1) reflects the fluorescence excitation laser and transmits the longer wavelengths emitted by the chromophore. The emitted light is filtered (EF) to efficiently select the emission spectrum and projected onto an EM CCD camera by the tube lens (TL). A motorized mirror (M) allows switching between brightfield and fluorescence microscopy.

The choice of well-separated wavelengths for trapping and fluorescence excitation is necessary for the efficient separation of the two laser beams through dichroic mirrors and filters. The use of a high quantum efficiency electron-multiplied CCD or sCMOS camera is essential to reach the high signal-to-noise ratios necessary for single chromophore detection.

5.6.5   Noise Isolation

Optical tweezers have the capability to measure subnanometer conformational changes of protein enzymes, but, as previously highlighted in Section 5.4.2, many sources of instrumental noise can deteriorate spatial resolution in optical tweezers. Electronic noise in the position detector can limit spatial resolution, but recent photodetectors and electronics allow reaching angstrom-level noise with several KHz bandwidth. Other sources of noise in position measurement are much more prominent and originate from mechanical oscillations, from thermal expansions and contractions in the microscope (thermal drifts), and from laser pointing and intensity instabilities. It is therefore of fundamental importance to isolate the experimental setup from any source of mechanical perturbation and, when this is not fully accomplishable, compensate those perturbations with active feedback systems. Several strategies have been developed in the last decade, using active or passive stabilization strategies, to limit instrumental noise and reach a spatial resolution that approaches the thermal noise limit.

Acoustic noise usually affects frequencies ranging from about 10 Hz to several KHz, while mechanical noise and thermal drifts usually affect lower frequencies. Acoustic noise may also be enhanced by resonances of the microscope mechanical structure or optics supports. The experimental setup is usually mounted on an optical table equipped with active isolators to limit mechanical vibrations. The microscope structure can be mounted over elastomers that absorb mechanical oscillations in the acoustic range of frequencies (Capitanio et al. 2005). Moreover, devices equipped with cooling fans should be put outside of the optical table and

the experimental setup should be placed in a room without direct air flow coming from air conditioning or other sources.

The laser trap is also affected by different sources of noise. Air turbulence deteriorates laser pointing stability and can be minimized by enclosing the laser beam path (Capitanio et al. 2005). Air in the laser path enclosure can be replaced with a low refractive index medium to further reduce turbulence (Abbondanzieri et al. 2005). Optical feedback, which generates light intensity fluctuations, can be limited by placing an optical isolator in the laser path near the laser source, as shown in Figure 5.19, or by passing the laser through an optical fiber and/or using active feedback systems (Carter et al. 2007).

Thermal drifts occur on a slow timescale and are quite difficult to reduce below the nanometer level by passive methods (i.e., temperature stabilization), which is really effective only when the whole room is stabilized at the sub-Kelvin level (Abbondanzieri et al. 2005). Otherwise, active feedback systems that compensate thermal drifts by moving the sample stage through piezoelectric translators are more beneficial and simple to implement (Capitanio et al. 2005; Carter et al. 2007). Box 5.3 describes a simple but effective feedback system that uses a video camera and a fiducial mark attached to the microscope coverslip to attain nanometer stabilization of the sample.

5.7   Optical Tweezers Impact in Biology

The last 20 years have seen astonishing progress in force measurements on biological systems, generated new paradigms on single protein function and opened new possibilities to investigate the complex mechanochemical regulation of cellular and molecular complexes. Optical tweezers have reached a spatial resolution of a few angstroms and temporal resolution of a few microseconds, which allowed elucidating details of the molecular mechanisms of molecular motors, DNA processing enzymes, RNA, and protein folding. Complex multiprotein interactions can now be investigated using a combination of single molecule manipulation and imaging tools. Precise pN sensitivity force measurements are now possible in living cells, opening the way to the study of a myriad of biological processes that are directly regulated by force or connected to the mechanical conditions of the cell and its surrounding environment.

5.7.1   High-Resolution Studies of Single Molecular Motors

Improvements in spatial resolution allowed researchers to probe the single steps of enzymatic reactions fundamental for life: transcription by RNA polymerase (RNAP) and translation by the ribosome. As reported in the previous sections, Abbondanzieri et al. developed an ultrastable optical trapping system with angstrom resolution, which they used to monitor transcriptional elongation by single molecules of *Escherichia coli* RNAP (Abbondanzieri et al. 2005) (Figure 5.7c). They showed that RNAP advances along DNA by discrete steps of 3.7 ± 0.6 Å, a distance consistent with the crystallographic spacing between neighboring base pairs in B-DNA. They also determined the force–velocity relationship for transcription and fits to these data were consistent with a Brownian ratchet model.

Box 5.3   Active Nanometer Stabilization Using a Video Camera

Eliminating thermal drifts and low-frequency noise in a microscope and optical tweezers setup is one of the most challenging tasks. A simple and effective way to get nanometer stability on long timescales is by using a bead stuck onto a coverslip surface as a fiducial mark to monitor drifts of the sample, and compensate them using a high-precision piezo stage capable of nanometer or subnanometer movements (Capitanio et al. 2005; Monico et al. 2014). The sample cell can be prepared by spreading micron-sized silica beads dissolved in a nitrocellulose solution onto a microscope coverslip and then attaching the coverslip to a microscope slide using double-stick tape. A silica bead should then be visualized with the focal plane of the objective positioned slightly above the bead and at large magnification to accurately sample its image with a CCD or CMOS camera. The bead image appears as represented in Figure 5.23 after image inversion and threshold
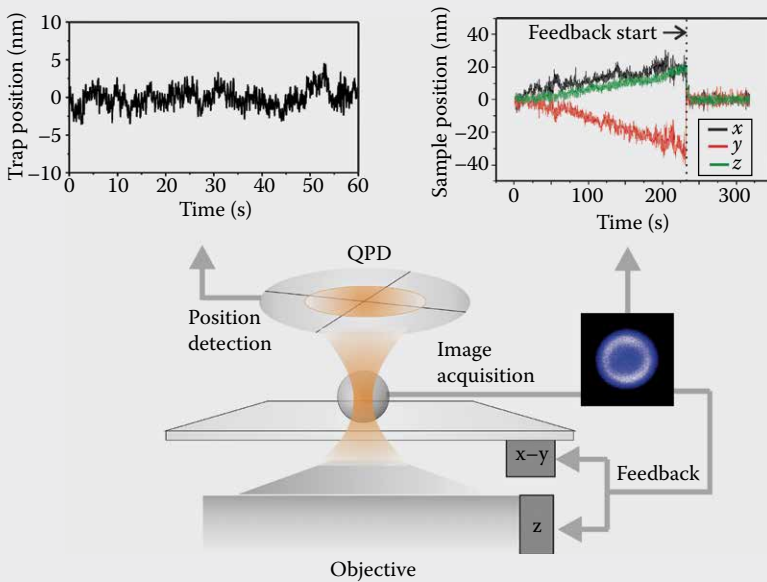
Figure 5.23 Nanometer stabilization of optical tweezers. A bead stuck onto the coverslip surface is used as a reference to monitor the sample position (top right graph), which normally drifts by several nanometers in a few minutes. A feedback system driving piezo translators stabilizes the sample to better than 1 nm. Movements of the trap relative to the sample can be monitored with the QPD (top left graph), when the trap is overlapped on the bead stuck onto the coverslip.

filtering to cut off the background noise outside the bead. The bead x and y coordinates can be obtained from the image centroid, while the z position can be obtained from the ratio between the intensity of the pixels inside the bead diffraction ring and those located outside. A feedback loop that acquires images of the bead, calculates x, y, and z coordinates, and sends a proportional correction signal to the piezo stage can thus compensate sample drifts. After proper calibration of the system and regulation of the feedback gain, the optical microscope can be stabilized to better than 1 nm using this approach (Capitanio et al. 2005) (see Figure 5.23). The range of noise frequencies on which the feedback system operates depends on the acquisition rate of the camera; for thermal drifts and low-frequency noise correction, a slow video-rate camera operating at 25 Hz is sufficient.

When performing optical tweezers experiments on surface-coupled molecules, it is also fundamental to check that the relative position of the feedback-stabilized sample and the optical traps is maintained at the nanometer level. To this end, an experimental procedure is represented in Figure 5.23: the trapping beam is positioned onto a surface-attached bead, which is stabilized by the feedback loop, and the relative movements of the laser and the bead are measured through the QPD. When the prescriptions described in Section 5.6.5 are fulfilled, nanometer stability can be achieved.

This breakthrough opened the way to detailed studies of the molecular mechanisms of RNAP and how gene expression is regulated during transcription. With the use of the same optical-trapping assay, Greenleaf et al. investigated folding of single nascent RNAs containing pbuE adenine riboswitch aptamers (Greenleaf et al. 2008). Riboswitches are important elements of mRNA structure that regulate genes through structural changes in ligand-binding RNA aptamers. In a recent study, Fazal et al. assembled a 32-protein, 1.5-megadalton preinitiation complex of RNA polymerase II, and observed subsequent initiation transcription processes in real time in a double-trap assay (Fazal et al. 2015). Recent studies demonstrate that it is possible to assemble complex macromolecules *in vitro* and investigate their properties with high resolution at a single molecule level.

Another set of extremely challenging experiments demonstrated the possibility of studying translation by the ribosome with optical tweezers (Figure 5.9b). Those experiments revealed that translation occurs through successive translocation-and-pause cycles, with each translocation step measuring three bases (i.e., one codon). This approach allowed investigating the dynamics of ribosome translation and analyzing the time the ribosome spends at each codon, thus revealing that there are three substeps in each step. Pause lengths, and thus the overall rate of translation, depend on the secondary structure of the mRNA, which is destabilized by an applied force, resulting in decrease of pause durations, but not of translocation times. The same group developed an experimental system to investigate the folding of single ribosome-bound stalled nascent

polypeptides with optical tweezers (Kaiser et al. 2011). This study directly showed that the ribosome affects protein folding and suggested that the ribosome not only decodes the genetic information and synthesizes polypeptides, but also promotes efficient attainment of the native state.

Improvements in temporal resolution allowed researchers to dissect the steps of chemomechanical transduction in a number of molecular motors, giving new insight into their mechanism of functioning. Myosin is one of the prototypical motor proteins, and it is involved in numerous biological processes such as muscle contraction, intracellular trafficking, cell movements, and signal transduction (Mermall et al. 1998). Skeletal muscle myosin is one of the most long-studied motor proteins, although a detailed analysis of its load dependence has been elusive for a long time to single molecule studies owing to its rapid chemomechanical cycle. Several principles of myosin function were first discovered on slower myosins belonging to different classes and, only recently, generalized to skeletal muscle myosin when new techniques with improved time resolution become available. In 1999, Veigel et al. demonstrated that myosin I, a widely expressed, single-headed, and membrane-associated motor produces its working stroke in two steps (Veigel et al. 1999). The second step of myosin, which was later discovered to be a common feature of the myosin family, regulates myosin kinetics through its load dependence and has emerged to play an important role in the functioning of different myosin (Batters and Veigel 2016). Myosin I was showed to respond to small resisting loads (<2 pN) by dramatically increasing the actin-attachment lifetime more than 75-fold (Laakso et al. 2008). This impressive tension sensitivity supports a role for myosin I as a molecular force sensor adapted to generate and sustain tension for extended time periods, rather than to rapidly transport cargos. On the contrary, myosin V is a double-headed efficient cargo transporter, and its high processivity has been explained by the load dependence of its second step (Veigel et al. 2005). In fact, when myosin V is attached to actin, intramolecular strain between the two myosin heads can significantly enhance the probability of the trail head detaching first, causing a strong increase in the number of forward steps over a system with no strain dependence. A second step was also observed in skeletal muscle myosin thanks to refinements in the temporal resolution of a three-bead assay (Capitanio et al. 2006). In that work, we demonstrated that the kinetics of this second step vary largely between different isoforms of skeletal muscle myosin, accounting for the variation, in different fiber types, of the rate of the cross-bridge cycle, which is tuned to the specific cellular function. Some years later we could finally find a technical solution to apply controlled loads to a single myosin molecule before the onset of its working stroke, thus opening the way to studies of load dependence of the complete myosin working stroke (Capitanio et al. 2012). In that paper, we could directly observe that the amplitude of the working stroke of skeletal muscle myosin is reduced by an opposing force, whereas its duration is slowed down at high ATP concentrations in a physiologic force range (<5 pN). These results support the idea that the contraction velocity of a single myosin molecule decreases with force–accordingly with the force-velocity curve of a whole muscle cell.

5.7.2   Combining Optical Manipulation and Imaging of Single Molecules

A further evolution of optical tweezers techniques consists in the development of a new generation of setups combining several single molecule methodologies to allow, for example, simultaneous single molecule localization using fluorescence microscopy and manipulation with optical tweezers. The first examples of these types of combined technologies consisted of a laser tweezers apparatus used to manipulate a biopolymer (e.g., DNA or actin) combined with an evanescent wave used for excitation and detection of single fluorophores. These setups were used to simultaneously measure mechanical output and ATPase reaction in single myosin molecules (Ishijima et al. 1998), or to image and measure the interactions of RNA polymerase (fluorescently labeled) with a DNA molecule suspended between two optical traps (Harada et al. 1999). These pioneering works combined manipulation of single molecules with detection of single chromophores. The technological developments in video camera sensitivity, allowed some years later the combination of optical tweezers with fluorescence imaging with 1 nm accuracy (FIONA) (Capitanio et al. 2007b). A growing set of tools combining optical tweezers with wide-field fluorescence microscopy techniques for the detection and localization of single molecules have been developed in the last years (Lang et al. 2004; Capitanio et al. 2007b; Monico et al. 2014). These tools have been mainly applied to the study of nucleic acids structure (Hohng et al. 2007; van Mameren et al. 2009) and DNA binding proteins and processing enzymes (Candelli et al. 2011; Zhou et al. 2011; Monico et al. 2014). More recently, different illumination configurations have been developed to selectively excite labeled proteins interacting with a DNA molecule suspended between two optically trapped beads. Comstock et al. developed a time-shared ultrahigh-resolution dual-optical trap interlaced with a confocal fluorescence microscope. The time-shared dual-optical trap was interlaced with a confocal fluorescence microscope, so that optical traps and fluorescence excitation were never both on simultaneously. This solution is useful to avoid enhanced photobleaching due to absorption of the near-infrared trapping light while the chromophore is in the excited state (Dijk et al. 2004). Thanks to this solution, they observed individual single fluorophore-labeled DNA oligonucleotides interacting with complementary DNA and coincident angstrom-scale changes in tether extension (Comstock et al. 2011). Heller et al. combined optical tweezers with stimulated emission depletion (STED) fluorescence microscopy. Proteins on DNA could be imaged with a resolution of 50 nm, a sixfold resolution improvement over that of confocal microscopy, allowing the visualization of individual DNA-binding proteins on densely covered DNA and in the presence of high protein concentrations.

5.7.3   Going Inside the Cell

Besides the numerous and fruitful applications of optical tweezers to the study of single biological molecules *in vitro*, optical tweezers have been applied to live-cell studies as well, and recent developments promise to further extend their usability in this area. Optical tweezers can be used as efficient tools to mechanically

stimulate cells or specific membrane proteins (Wang et al. 2005), measure mechanical properties of the cell (Choquet et al. 1997), quantify strength of molecular bonds between membrane proteins and binding partners (Litvinov et al. 2002), or investigate mechanical properties of molecular motors in living cells (Blehm et al. 2013). Several reviews illustrate the application of optical tweezers to live cells (Veigel and Schmidt 2011; Oddershede 2012).

Although manipulating cells from the outer membrane is the most common use, direct manipulation and force measurement inside living cells with optical tweezers have seen great progress recently. One of the main issues for quantitative force measurements in living cells with optical tweezers is the calibration of the trap stiffness k_{trap}. In fact, opposite to *in vitro* experiments or experiments on the cell membrane, in which the viscous properties of the medium are well known, experiments in living cells are complicated by the viscoelastic properties of the cytoplasm, which are *a priori* unknown. Another major problem in this kind of experiment is the variable size of endogenous lipid droplets and vesicles that are usually employed as force probes. Since k_{trap} varies largely with size in the micrometer to submicrometer range (see Table 5.1), it is extremely difficult to precisely calibrate traps for cargoes of unknown size. Barak et al. developed a calibration method to precisely measure the force generated by motor proteins on single cargos of unknown size in cell extracts (Barak et al. 2013). Rai et al. recently demonstrated optical trapping at single molecule resolution inside cells (Rai et al. 2013). They used phagocytosed latex beads of uniform size to circumvent the calibration uncertainty. Fischer et al. developed a calibration method that allows obtaining all the unknown variables for a correct calibration of optical tweezers inside cells (Fischer and Berg-Sorensen 2007; Fischer et al. 2010). Two recent articles exploited and further extended this technique to measure stall force of dynein and kinesin *in vivo*. Hendricks et al. developed a calibration method taking into account any variations among cargoes and local viscoelastic properties of the cytoplasm. They examined latex beads phagocytosed into living mammalian macrophages and found great differences in the characteristics of forces generated by teams of plus- (kinesin) and minus- (dynein) end–directed motors (Hendricks et al. 2012). Blehm et al. used a method that allows *in vivo* calibration of optical tweezers on lipid vesicles and phagocytosed polystyrene beads to study kinesin and dynein stall forces during intracellular transport (Blehm et al. 2013).

References

Abbondanzieri EA, Greenleaf WJ, Shaevitz JW, Landick R, Block SM (2005) Direct observation of base-pair stepping by RNA polymerase. *Nature* 438:460–465.

Allersma MW, Gittes F, deCastro MJ, Stewart RJ, Schmidt CF (1998) Two-dimensional tracking of ncd motility by back focal plane interferometry. *Biophys J* 74:1074–1085.

Arya M, Kolomeisky AB, Romo GM, Cruz MA, Lopez JA, Anvari B (2005) Dynamic force spectroscopy of glycoprotein Ib-IX and von Willebrand factor. *Biophys J* 88:4391–4401.

Ashkin A (1992) Forces of a single-Beam gradient laser trap on a dielectric sphere in the ray optics regime. *Biophys J* 61:569–582.

Ashkin A, Dziedzik JM, Bjorkholm JE, Chu S (1986) Observation of a single-Beam gradient force optical trap for dielectric particles. *Opt Lett* 11:288–290.

Barak P, Rai A, Rai P, Mallik R (2013) Quantitative optical trapping on single organelles in cell extract. *Nat Meth* 10:68–70.

Batchelor GK (1967) *An introduction to fluid dynamics.* Cambridge: U.P.

Batters C, Veigel C (2016) Mechanics and activation of unconventional myosins. *Traffic* 17:860–871.

Berg OG, Winter RB, von Hippel PH (1981) Diffusion-driven mechanisms of protein translocation on nucleic acids. 1. Models and theory. *Biochemistry* 20:6929–6948.

Bianco P, Bongini L, Melli L, Dolfi M, Lombardi V (2011) PicoNewton-millisecond force steps reveal the transition kinetics and mechanism of the double-stranded DNA elongation. *Biophys J* 101:866–874.

Bianco P, Nagy A, Kengyel A, Szatmari D, Martonfalvi Z, Huber T, Kellermayer MS (2007) Interaction forces between F-actin and titin PEVK domain measured with optical tweezers. *Biophys J* 93:2102–2109.

Blehm BH, Schroer TA, Trybus KM, Chemla YR, Selvin PR (2013) In vivo optical trapping indicates kinesin's stall force is reduced by dynein during intracellular transport. *Proc Natl Acad Sci U S A* 110:3381–3386.

Buckley CD, Tan JY, Anderson KL, Hanein D, Volkmann N, Weis WI, Nelson WJ, Dunn AR (2014) The minimal cadherin-catenin complex binds to actin filaments under force. *Science* 346:1254211.

Candelli A, Wuite GJ, Peterman EJ (2011) Combining optical trapping, fluorescence microscopy and micro-Fluidics for single molecule studies of DNA-protein interactions. *Phys Chem Chem Phys: PCCP* 13:7263–7272.

Capitanio M, Canepari M, Cacciafesta P, Lombardi V, Cicchi R, Maffei M, Pavone FS, Bottinelli R (2006) Two independent mechanical events in the interaction cycle of skeletal muscle myosin with actin. *Proc Natl Acad Sci U S A* 103:87–92.

Capitanio M, Canepari M, Maffei M, Beneventi D, Monico C, Vanzi F, Bottinelli R, Pavone FS (2012) Ultrafast force-clamp spectroscopy of single molecules reveals load dependence of myosin working stroke. *Nat Meth* 9:1013–1019.

Capitanio M, Cicchi R, Pavone FS (2005) Position control and optical manipulation for nanotechnology applications. *Eur Phys J B* 46:1–8.

Capitanio M, Cicchi R, Pavone FS (2007a) Continuous and time-shared multiple optical tweezers for the study of single motor proteins. *Optics Lasers Eng* 45:450–457.

Capitanio M, Maggi D, Vanzi F, Pavone F (2007b) Fiona in the trap: The advantages of combining optical tweezers and fluorescence. *J Opt A: Pure Appl Opt* 9:S157.

Capitanio M, Pavone FS (2013) Interrogating biology with force: Single molecule high-resolution measurements with optical tweezers. *Biophys J* 105:1293–1303.

Capitanio M, Romano G, Ballerini R, Giuntini M, Pavone FS, Dunlap D, Finzi L (2002) Calibration of optical tweezers with differential interference contrast signals. *Review Sci Instrum* 73:1687–1696.

Capitanio M, Vanzi F, Broggio C, Cicchi R, Normanno D, Romano G, Sacconi L, Pavone FS (2004) Exploring molecular motors and switches at the single-molecule level. *Micr Res Tech* 65:194–204.

Carter AR, King GM, Ulrich TA, Halsey W, Alchenberger D, Perkins TT (2007) Stabilization of an optical microscope to 0.1 nm in three dimensions. *Appl Opt* 46:421–427.

Carter AR, Seol Y, Perkins TT (2009) Precision surface-Coupled optical-Trapping assay with one-Basepair resolution. *Biophys J* 96:2926–2934.

Carter BC, Vershinin M, Gross SP (2008) A comparison of step-detection methods: How well can you do? *Biophys J* 94:306–319.

Carter NJ, Cross RA (2005) Mechanics of the kinesin step. *Nature* 435:308–312.

Cecconi C, Shank EA, Bustamante C, Marqusee S (2005) Direct observation of the three-state folding of a single protein molecule. *Science* 309: 2057–2060.

Chemla YR, Aathavan K, Michaelis J, Grimes S, Jardine PJ, Anderson DL, Bustamante C (2005) Mechanism of force generation of a viral DNA packaging motor. *Cell* 122:683–692.

Chen C, Greenberg MJ, Laakso JM, Ostap EM, Goldman YE, Shuman H (2012) Kinetic schemes for post-synchronized single molecule dynamics. *Biophys J* 102:L23–L25.

Cheng W, Arunajadai SG, Moffitt JR, Tinoco I, Jr., Bustamante C (2011) Single-base pair unwinding and asynchronous RNA release by the hepatitis C virus NS3 helicase. *Science* 333:1746–1749.

Cheng W, Hou X, Ye F (2010) Use of tapered amplifier diode laser for biological-friendly high-Resolution optical trapping. *Opt Lett* 35:2988–2990.

Choquet D, Felsenfeld DP, Sheetz MP (1997) Extracellular matrix rigidity causes strengthening of integrin-Cytoskeleton linkages. *Cell* 88:39–48.

Comstock MJ, Ha T, Chemla YR (2011) Ultrahig-resolution optical trap with single-fluorophore sensitivity. *Nat Meth* 8:335–340.

Curtis JE, Koss BA, Grier DG (2002) Dynamic holographic optical tweezers. *Opt Commun* 207:169–175.

Dame RT, Noom MC, Wuite GJL (2006) Bacterial chromatin organization by H-NS protein unravelled using dual DNA manipulation. *Nature* 444:387–390.

de Messieres M, Chang JC, Brawn-Cinani B, La Porta A (2012) Single-Molecule study of G-Quadruplex disruption using dynamic force spectroscopy. *Phys Rev Lett* 109:058101.

deCastro MJ, Fondecave RM, Clarke LA, Schmidt CF, Stewart RJ (2000) Working strokes by single molecules of the kinesin-related microtubule motor ncd. *Nat Cell Biol* 2:724–729.

Dienerowitz M, Mazilu M, Dholakia K (2008) Optical manipulation of nanoparticles: A review. *J Nanophotonics* 2:021875.

Dijk MA, Kapitein LC, Mameren J, Schmidt CF, Peterman EJ (2004) Combining optical trapping and single-molecule fluorescence spectroscopy: Enhanced photobleaching of fluorophores. *J Phys Chem B* 108:6479–6484.

Dudko OK, Hummer G, Szabo A (2008) Theory, analysis, and interpretation of single-molecule force spectroscopy experiments. *Proc Natl Acad Sci U S A* 105:15755–15760.

Dufresne ER, Grier DG (1998) Optical tweezer arrays and optical substrates created with diffractive optics. *Review Sci Instrum* 69:1974–1977.

Dufresne ER, Spalding GC, Dearing MT, Sheets SA, Grier DG (2001) Computer-generated holographic optical tweezer arrays. *Review Sci Instrum* 72:1810–1816.

Dumont S, Cheng W, Serebrov V, Beran RK, Tinoco I, Pyle AM, Bustamante C (2006) RNA translocation and unwinding mechanism of HCVNS3 helicase and its coordination by ATP. *Nature* 439:105–108.

Elms PJ, Chodera JD, Bustamante CJ, Marqusee S (2012) Limitations of constant-force-feedback experiments. *Biophys J* 103:1490–1499.

Evans E (2001) Probing the relation between force - Lifetime - and chemistry in single molecular bonds. *Annu Rev Bioph Biom* 30:105–128.

Fallman E, Axner O (1997) Design for fully steerable dual-trap optical tweezers. *Appl Opt* 36:2107–2113.

Fazal FM, Meng CA, Murakami K, Kornberg RD, Block SM (2015) Real-time observation of the initiation of RNA polymerase II transcription. *Nature* 525:274–277.

Finer JT, Simmons RM, Spudich JA (1994) Single myosin molecule mechanics: Piconewton forces and nanometer steps. *Nature* 368:113–119.

Fischer M, Berg-Sorensen K (2007) Calibration of trapping force and response function of optical tweezers in viscoelastic media. *J Opt a-Pure Appl Op* 9:S239–S250.

Fischer M, Richardson AC, Reihani SN, Oddershede LB, Berg-Sorensen K (2010) Active-passive calibration of optical tweezers in viscoelastic media. *Review Sci Instrum* 81:015103.

Garcia-Garcia C, Frieda KL, Feoktistova K, Fraser CS, Block SM (2015) Factor-dependent processivity in human eIF4A DEAD-box helicase. *Science* 348:1486–1488.

Gebhardt JC, Bornschlogl T, Rief M (2010) Full distance-resolved folding energy landscape of one single protein molecule. *Proc Natl Acad Sci U S A* 107:2013–2018.

Ghislain L, Switz NA, Webb WW (1994) Measurement of small forces using an optical trap. *Rev Sci Instrum* 65:2762–2768.

Gittes F, Schmidt CF (1998a) Thermal noise limitations on micromechanical experiments. *Eur Biophys J Biophy* 27:75–81.

Gittes F, Schmidt CF (1998b) Signals and noise in micromechanical measurements. *Meth Cell Biol* 55:129–156.

Gittes F, Schmidt CF (1998c) Interference model for back-focal-plane displacement detection in optical tweezers. *Optics Lett* 23:7–9.

Greenberg MJ, Lin T, Goldman YE, Shuman H, Ostap EM (2012) Myosin IC generates power over a range of loads via a new tension-sensing mechanism. *Proc Natl Acad Sci U S A* 109:E2433–E2440.

Greenberg MJ, Shuman H, Ostap EM (2014) Inherent force-Dependent properties of beta-Cardiac myosin contribute to the force-Velocity relationship of cardiac muscle. *Biophys J* 107:L41–L44.

Greenleaf WJ, Frieda KL, Foster DA, Woodside MT, Block SM (2008) Direct observation of hierarchical folding in single riboswitch aptamers. *Science* 319:630–633.

Greenleaf WJ, Woodside MT, Block SM (2007) High-resolution, single-molecule measurements of biomolecular motion. *Annu Rev Biophys Biomol Struct* 36:171–190.

Greenleaf WJ, Woodside MT, Abbondanzieri EA, Block SM (2005) Passive all-optical force clamp for high-resolution laser trapping. *Phys Rev Lett* 95:208102.

Grier DG (2003) A revolution in optical manipulation. *Nature* 424:810–816.

Guilford WH, Tournas JA, Dascalu D, Watson DS (2004) Creating multiple time-shared laser traps with simultaneous displacement detection using digital signal processing hardware. *Anal Biochem* 326:153–166.

Guo B, Guilford WH (2006) Mechanics of actomyosin bonds in different nucleotide states are tuned to muscle contraction. *Proc Natl Acad Sci U S A* 103:9844–9849.

Hansen PM, Tolic-Norrelykke IM, Flyvbjerg H, Berg-Sorensen K (2006) Tweezercalib 2.1: Faster version of MatLab package for precise calibration of optical tweezers. *Comput Phys Commun* 175:572–573.

Harada Y, Funatsu T, Murakami K, Nonoyama Y, Ishihama A, Yanagida T (1999) Single-Molecule imaging of RNA polymerase-DNA interactions in real time. *Biophys J* 76:709–715.

Hecht E (2002) *Optics.* 4th Edition. Reading, MA: Addison-Wesley.

Hendricks AG, Holzbaur EL, Goldman YE (2012) Force measurements on cargoes in living cells reveal collective dynamics of microtubule motors. *Proc Natl Acad Sci U S A* 109:18447–18452.

Hohng S, Zhou R, Nahas MK, Yu J, Schulten K, Lilley DM, Ha T (2007) Fluorescence-force spectroscopy maps two-dimensional reaction landscape of the holliday junction. *Science* 318:279–283.

Howard J (2001) Mechanics of motor proteins and the cytoskeleton. MA: Sinauer Associates, Inc. Publisher, Sunderland, MA.

Hulst HCvd (1981) *Light scattering by small particles.* New York, NY: Dover Publications.

Ishijima A, Kojima H, Funatsu T, Tokunaga M, Higuchi H, Tanaka H, Yanagida T (1998) Simultaneous observation of individual ATPase and mechanical events by a single myosin molecule during interaction with actin. *Cell* 92:161–171.

Iwaki M, Iwane AH, Shimokawa T, Cooke R, Yanagida T (2009) Brownian search-and-catch mechanism for myosin-VI steps. *Nat Chem Biol* 5:403–405.

Jaalouk DE, Lammerding J (2009) Mechanotransduction gone awry. *Nat Rev Mol Cell Biol* 10:63–73.

Kaiser CM, Goldman DH, Chodera JD, Tinoco I, Bustamante C (2011) The ribosome modulates nascent protein folding. *Science* 334:1723–1727.

Kim J, Zhang CZ, Zhang X, Springer TA (2010) A mechanically stabilized receptor-ligand flex-bond important in the vasculature. *Nature* 466: 992–995.

Knight AE, Veigel C, Chambers C, Molloy JE (2001) Analysis of single-molecule mechanical recordings: Application to acto-myosin interactions. *Prog Biophys Mol Biol* 77:45–72.

Laakso JM, Lewis JH, Shuman H, Ostap EM (2008) Myosin I can act as a molecular force sensor. *Science* 321:133–136.

Laakso JM, Lewis JH, Shuman H, Ostap EM (2010) Control of myosin-I force sensing by alternative splicing. *Proc Natl Acad Sci U S A* 107:698–702.

Landau LD, Lifshiĭ̄s EM, Pitaevskiĭ LP (1980) *Statistical physics*, 3d rev. and enl. Edition. Oxford; New York: Pergamon Press.

Lang MJ, Asbury CL, Shaevitz JW, Block SM (2002) An automated two-dimensional optical force clamp for single molecule studies. *Biophys J* 83:491–501.

Lang MJ, Fordyce PM, Engh AM, Neuman KC, Block SM (2004) Simultaneous, coincident optical trapping and single-molecule fluorescence. *Nat Meth* 1:133–139.

Lewalle A, Steffen W, Stevenson O, Ouyang Z, Sleep J (2008) Single-Molecule measurement of the stiffness of the rigor myosin head. *Biophys J* 94:2160–2169.

Liesener J, Reicherter M, Haist T, Tiziani HJ (2000) Multi-functional optical tweezers using computer-generated holograms. *Opt Commun* 185:77–82.

Liphardt J, Onoa B, Smith SB, Tinoco IJ, Bustamante C (2001) Reversible unfolding of single RNA molecules by mechanical force. *Science* 292:733–737.

Litvinov RI, Shuman H, Bennett JS, Weisel JW (2002) Binding strength and activation state of single fibrinogen-integrin pairs on living cells. *Proc Natl Acad Sci U S A* 99:7426–7431.

Marshall BT, Long M, Piper JW, Yago T, McEver RP, Zhu C (2003) Direct observation of catch bonds involving cell-adhesion molecules. *Nature* 423:190–193.

Mermall V, Post PL, Mooseker MS (1998) Unconventional myosins in cell movement, membrane traffic, and signal transduction. *Science* 279:527–533.

Mio C, Gong T, Terray A, Marr WM (2000) Design of a scanning laser optical trap for multiparticle manipulation. *Rev Sci Instrum* 71:2196–2200.

Moffitt JR, Chemla YR, Izhaky D, Bustamante C (2006) Differential detection of dual traps improves the spatial resolution of optical tweezers. *Proc Natl Acad Sci U S A* 103:9006–9011.

Moffitt JR, Chemla YR, Smith SB, Bustamante C (2008) Recent advances in optical tweezers. *Ann Rev Biochem* 77:205–228.

Molloy JE, Burns JE, Kendrick-Jones J, Tregear RT, White DCS (1995) Movement and force produced by a single myosin head. *Nature* 378:209–212.

Monico C, Belcastro G, Vanzi F, Pavone FS, Capitanio M (2014) Combining single-molecule manipulation and imaging for the study of protein–DNA interactions. *J Vis Exp: JoVE* 90:51446.

Monico C, Capitanio M, Belcastro G, Vanzi F, Pavone FS (2013) Optical methods to study protein–DNA interactions in vitro and in living cells at the single-Molecule level. *Int J Mol Sci* 14:3961–3992.

Nambiar R, Gajraj A, Meiners JC (2004) All-optical constant-force laser tweezers. *Biophys J* 87:1972–1980.

Nambiar R, Meiners JC (2002) Fast position measurements with scanning line optical tweezers. *Opt Lett* 27:836–838.

Neuman KC, Block SM (2004) Optical trapping. *Rev Sci Instrum* 75:2787–2809.

Neuman KC, Chadd EH, Liou GF, Bergman K, Block SM (1999) Characterization of photodamage to Escherichia coli in optical traps. *Biophys J* 77:2856–2863.

Neuman KC, Nagy A (2008) Single-molecule force spectroscopy: optical tweezers, magnetic tweezers and atomic force microscopy. *Nat Meth* 5:491–505.

Nishiyama M, Muto E, Inoue Y, Yanagida T, Higuchi H (2001) Substeps within the 8-nm step of the ATPase cycle of single kinesin molecules. *Nat Cell Biol* 3:425–428.

Noom MC, van den Broek B, van Mameren J, Wuite GJ (2007) Visualizing single DNA-bound proteins using DNA as a scanning probe. *Nat Meth* 4:1031–1036.

Oddershede LB (2012) Force probing of individual molecules inside the living cell is now a reality. *Nat Chem Biol* 8:879–886.

Osterman N (2010) TweezPal - Optical tweezers analysis and calibration software. *Comput Phys Commun* 181:1911–1916.

Piazzesi G, Reconditi M, Linari M, Lucii L, Sun YB, Narayanan T, Boesecke P, Lombardi V, Irving M (2002) Mechanism of force generation by myosin heads in skeletal muscle. *Nature* 415:659–662.

Pralle A, Prummer M, Florin EL, Stelzer EH, Horber JK (1999) Three-dimensional high-resolution particle tracking for optical tweezers by forward scattered light. *Microsc Res Tech* 44:378–386.

Pyrpassopoulos S, Shuman H, Ostap EM (2010) Single-Molecule adhesion forces and attachment lifetimes of myosin-I phosphoinositide interactions. *Biophys J* 99:3916–3922.

Rai AK, Rai A, Ramaiya AJ, Jha R, Mallik R (2013) Molecular adaptations allow dynein to generate large collective forces inside cells. *Cell* 152:172–182.

Reconditi M, Linari M, Lucii L, Stewart A, Sun YB, Boesecke P, Narayanan T, et al. (2004) The myosin motor in muscle generates a smaller and slower working stroke at higher load. *Nature* 428:578–581.

Ren KF, Grehan G, Gouesbet G (1996) Prediction of reverse radiation pressure by generalized Lorenz-Mie theory. *Appl Opt* 35:2702–2710.

Ren Y, Effler JC, Norstrom M, Luo T, Firtel RA, Iglesias PA, Rock RS, Robinson DN (2009) Mechanosensing through cooperative interactions between myosin II and the actin crosslinker cortexillin I. *Curr Biol* 19:1421–1428.

Rief M, Rock RS, Mehta AD, Mooseker MS, Cheney RE, Spudich JA (2000) Myosin-V stepping kinetics: A molecular model for processivity. *Proc Natl Acad Sci U S A* 97:9482–9486.

Rock RS, Rice SE, Wells AL, Purcell TJ, Spudich JA, Sweeney HL (2001) Myosin VI is a processive motor with a large step size. *Proc Natl Acad Sci U S A* 98:13655–13659.

Rognoni L, Stigler J, Pelz B, Ylanne J, Rief M (2012) Dynamic force sensing of filamin revealed in single-Molecule experiments. *Proc Natl Acad Sci U S A* 109:19679–19684.

Sasaki K, Masanori M, Misawa H, Kitamura N, Masuhara H (1991) Pattern formation and flow control of fine particles by laser-scanning micromanipulation. *Opt Lett* 16:1463–1465.

Skinner GM, Baumann CG, Quinn DM, Molloy JE, Hoggett JG (2004) Promoter binding, initiation, and elongation by bacteriophage T7 RNA polymerase. *A single-molecule view of the transcription cycle. J Biol Chem* 279:3239–3244.

Smith DA (1998) Direct tests of muscle cross-bridge theories: Predictions of a Brownian dumbbell model for position-dependent cross-bridge lifetimes and step sizes with an optically trapped actin filament. *Biophys J* 75:2996–3007.

Smith DA, Steffen W, Simmons RM, Sleep J (2001a) Hidden-Markov methods for the analysis of single-molecule actomyosin displacement data: The variance-Hidden-Markov method. *Biophys J* 81:2795–2816.

Smith DE, Tans SJ, Smith SB, Grimes S, Anderson DL, Bustamante C (2001b) The bacteriophage phi 29 portal motor can package DNA against a large internal force. *Nature* 413:748–752.

Smith SB, Cui Y, Bustamante C (1996) Overstretching B-DNA: The elastic response of individual double-stranded and single-stranded DNA molecules. *Science* 271:795–799.

Smith SP, Bhalotra SR, Brody AL, Brown BL, Boyda EK, Prentiss M (1999) Inexpensive optical tweezers for undergraduate laboratories. *Am J Phys* 67:26–35.

Steffen W, Smith D, Simmons R, Sleep J (2001) Mapping the actin filament with myosin. *Proc Natl Acad Sci U S A* 98:14949–14954.

Stigler J, Ziegler F, Gieseke A, Gebhardt JC, Rief M (2011) The complex folding network of single calmodulin molecules. *Science* 334:512–516.

Svoboda K, Block SM (1994) Force and velocity measured for single kinesin molecules. *Cell* 77:773–784.

Svoboda K, Schmidt CF, Schnapp BJ, Block SM (1993) Direct observation of kinesin stepping by optical trapping interferometry. *Nature* 365:721–727.

Takagi Y, Homsher EE, Goldman YE, Shuman H (2006) Force generation in single conventional actomyosin complexes under high dynamic load. *Biophys J* 90:1295–1307.

Uemura S, Higuchi H, Olivares AO, De La Cruz EM, Ishiwata S (2004) Mechanochemical coupling of two substeps in a single myosin V motor. *Nat Struct Mol Biol* 11:877–883.

Valentine MT, Guydosh NR, Gutierrez-Medina B, Fehr AN, Andreasson JO, Block SM (2008) Precision steering of an optical trap by electro-optic deflection. *Opt Lett* 33:599–601.

van Mameren J, Gross P, Farge G, Hooijman P, Modesti M, Falkenberg M, Wuite GJ, Peterman EJ (2009) Unraveling the structure of DNA during overstretching by using multicolor, single-molecule fluorescence imaging. *Proc Natl Acad Sci U S A* 106:18231–18236.

Veigel C, Coluccio LM, Jontes JD, Sparrow JC, Milligan RA, Molloy JE (1999) The motor protein myosin-I produces its working stroke in two steps. *Nature* 398:530–533.

Veigel C, Molloy JE, Schmitz S, Kendrick-Jones J (2003) Load-dependent kinetics of force production by smooth muscle myosin measured with optical tweezers. *Nat Cell Biol* 5:980–986.

Veigel C, Schmidt CF (2011) Moving into the cell: Single-molecule studies of molecular motors in complex environments. *Nat Rev Mol Cell Biol* 12:163–176.

Veigel C, Schmitz S, Wang F, Sellers JR (2005) Load-dependent kinetics of myosin-V can explain its high processivity. *Nat Cell Biol* 7:861–869.

Veigel C, Wang F, Bartoo ML, Sellers JR, Molloy JE (2002) The gated gait of the processive molecular motor, myosin V. *Nat Cell Biol* 4:59–65.

Visscher K, Gross SP, Block SM (1996) Construction of multiple-beam optical traps with nanometer-resolution position sensing. *IEEE J Sel Top Quant Electron* 2:1066–1076.

Visscher K, Schnitzer MJ, Block SM (1999) Single kinesin molecules studied with a molecular force clamp. *Nature* 400:184–189.

Walter WJ, Brenner B, Steffen W (2010) Cytoplasmic dynein is not a conventional processive motor. *J Struct Biol* 170:266–269.

Walter WJ, Koonce MP, Brenner B, Steffen W (2012) Two independent switches regulate cytoplasmic dynein's processivity and directionality. *Proc Natl Acad Sci U S A* 109:5289–5293.

Wang MD, Schnitzer MJ, Yin H, Landick R, Gelles J, Block SM (1998) Force and velocity measured for single molecules of RNA polymerase. *Science* 282:902–907.

Wang Y, Botvinick EL, Zhao Y, Berns MW, Usami S, Tsien RY, Chien S (2005) Visualizing the mechanical activation of Src. *Nature* 434:1040–1045.

Wen JD, Lancaster L, Hodges C, Zeri AC, Yoshimura SH, Noller HF, Bustamante C, Tinoco I (2008) Following translation by single ribosomes one codon at a time. *Nature* 452:598–603.

Woodside MT, Anthony PC, Behnke-Parks WM, Larizadeh K, Herschlag D, Block SM (2006) Direct measurement of the full, sequence-dependent folding landscape of a nucleic acid. *Science* 314:1001–1004.

Wozniak MA, Chen CS (2009) Mechanotransduction in development: A growing role for contractility. *Nat Rev Mol Cell Biol* 10:34–43.

Wright WH, Sonek GJ, Berns MW (1994) Parametric study of the forces on microspheres held by optical tweezers. *Appl Opt* 33:1735–1748.

Wuite GJ, Smith SB, Young M, Keller D, Bustamante C (2000) Single-molecule studies of the effect of template tension on T7 DNA polymerase activity. *Nature* 404:103–106.

Yin H, Wang MD, Svoboda K, Landick R, Block SM, Gelles J (1995) Transcription against an applied force. *Science* 270:1653–1657.

Zhou R, Kozlov AG, Roy R, Zhang J, Korolev S, Lohman TM, Ha T (2011) SSB functions as a sliding platform that migrates on DNA via reptation. *Cell* 146:222–232.

Index